

1 **Impacts of Global Open Fire Aerosols on Direct Radiative, Cloud**  
2 **and Surface-Albedo Effects Simulated with CAM5**

3  
4 Yiquan Jiang<sup>1,2</sup>, Zheng Lu<sup>2</sup>, Xiaohong Liu<sup>2\*</sup>, Yun Qian<sup>3</sup>, Kai Zhang<sup>3</sup>, Yuhang Wang<sup>4</sup>  
5 and Xiu-Qun Yang<sup>1</sup>  
6

7  
8 <sup>1</sup> *CMA-NJU Joint Laboratory for Climate Prediction Studies, Institute for Climate*  
9 *and Global Change Research, School of Atmospheric Sciences, Nanjing University,*  
10 *Nanjing, China*

11  
12 <sup>2</sup> *Department of Atmospheric Science, University of Wyoming*

13  
14 <sup>3</sup> *Pacific Northwest National Laboratory, Richland, Washington, USA*

15  
16 <sup>4</sup> *School of Earth and Atmospheric Sciences, Georgia Institute of Technology, Atlanta,*  
17 *Georgia, USA*

18  
19  
20  
21 \*Corresponding author:

22  
23 Dr. Xiaohong Liu  
24 Department of Atmospheric Science  
25 University of Wyoming  
26 Laramie, WY 82071  
27 Phone (307) 766-3225  
28 E-mail: xliu6@uwyo.edu  
29

30 **Abstract**

31 Aerosols from open-land fires could significantly perturb the global radiation  
32 balance and induce the climate change. In this study, Community Atmospheric Model  
33 version 5 (CAM5) with prescribed daily fire aerosol emissions is used to investigate  
34 the spatial and seasonal characteristics of radiative effects (REs, relative to the case of  
35 no fires) of open fire aerosols including black carbon (BC) and particulate organic  
36 matter (POM) from 2003 to 2011. The global annual mean RE due to  
37 aerosol-radiation interactions (RE<sub>ari</sub>) of all fire aerosols is  $0.16 \pm 0.01 \text{ W m}^{-2}$  ( $1\sigma$   
38 uncertainty), mainly due to the absorption of fire BC ( $0.25 \pm 0.01 \text{ W m}^{-2}$ ), while fire  
39 POM induces a small overall effect ( $-0.05 \text{ W m}^{-2}$  and  $0.04 \pm 0.01 \text{ W m}^{-2}$ , respectively  
40 based on two methods). Strong positive RE<sub>ari</sub> is found in the Arctic and in the  
41 oceanic regions west of southern Africa and South America as a result of amplified  
42 absorption of fire BC above low-level clouds, in general agreement with satellite  
43 observations. The global annual mean RE due to aerosol-cloud interactions (RE<sub>aci</sub>) of  
44 all fire aerosols is  $-0.70 \pm 0.05 \text{ W m}^{-2}$ , resulting mainly from the fire POM effect  
45 ( $-0.59 \pm 0.03 \text{ W m}^{-2}$ ). RE<sub>ari</sub> ( $0.43 \pm 0.03 \text{ W m}^{-2}$ ) and RE<sub>aci</sub> ( $-1.38 \pm 0.23 \text{ W m}^{-2}$ ) in the  
46 Arctic are stronger than those in the tropics ( $0.17 \pm 0.02$  and  $-0.82 \pm 0.09 \text{ W m}^{-2}$ ,  
47 respectively for RE<sub>ari</sub> and RE<sub>aci</sub>), although the fire aerosol burden is higher in the  
48 tropics. The large cloud liquid water path over land areas and low solar zenith angle  
49 of the Arctic favor the strong fire aerosol RE<sub>aci</sub> (up to  $-15 \text{ W m}^{-2}$ ) during the Arctic  
50 summer. Significant surface cooling, precipitation reduction and low-level cloud  
51 amount increase are also found in the Arctic summer as a result of the fire aerosol  
52 RE<sub>aci</sub> based on the atmosphere-only simulations. The global annual mean RE due to

53 surface albedo changes (RE<sub>fac</sub>) over land areas ( $0.03 \pm 0.10 \text{ W m}^{-2}$ ) is small and  
54 statistically insignificant, and is mainly due to the fire BC-in-snow effect ( $0.02 \text{ W m}^{-2}$ )  
55 with the maximum albedo effect occurring in spring ( $0.12 \text{ W m}^{-2}$ ) when snow starts to  
56 melt.

57

## 58 **1. Introduction**

59 Open fires or biomass burning of living and dead vegetation are an integral  
60 component of the Earth system, and have significant impacts on the carbon cycle  
61 [*Ciais et al.*, 2013] and the climate [*Bowman et al.*, 2009; *Keywood et al.*, 2011; *Liu et*  
62 *al.*, 2014; *Sommers et al.*, 2014; *Voulgarakis and Field*, 2015]. On one hand, open  
63 fires can perturb the climate system by emitting greenhouse gases and aerosols  
64 [*Kaiser et al.*, 2012; *Wiedinmyer et al.*, 2011]. On the other hand, climate states and  
65 variabilities can play a critical role in determining the occurrence frequency and  
66 intensity of open fires [*Marlon et al.*, 2009; *van der Werf et al.*, 2008; *Westerling et*  
67 *al.*, 2006; *Bistinas et al.*, 2014]. However, there are still large unknowns regarding the  
68 feedback mechanisms between open fire and climate interactions [*Carslaw et al.*,  
69 2010; *Liu et al.*, 2014]. A qualification of radiative forcing of fire aerosols as  
70 conducted in this study is the first step to reduce these uncertainties.

71 Particles emitted from open fires can exert significant perturbations to the  
72 climate system by scattering and absorbing the solar radiation in the atmosphere (i.e.,  
73 direct effect) [*Carslaw et al.*, 2010] and by changing the surface albedo when they are  
74 deposited on the snow and ice (i.e., surface albedo effect) [*Flanner et al.*, 2007; *Quinn*  
75 *et al.*, 2008; *Randerson et al.*, 2006; *Qian et al.*, 2011, 2015]. In addition, open fire or

76 smoke particles can modify the cloud properties, precipitation efficiency, and the  
77 hydrological cycle by changing the atmospheric thermal structure (i.e., semi-direct  
78 effect) [*Koch and Del Genio, 2010; Andreae et al., 2004b*] or acting as cloud  
79 condensation nuclei (CCN) (i.e., indirect effects) [*Andreae and Rosenfeld, 2008; Qian*  
80 *et al., 2009; Lu and Sokolik, 2013*].

81 The radiative effect (RE) [*Boucher and Tanre, 2000*] and radiative forcing (RF)  
82 [*Forster et al., 2007; Myhre et al., 2013a*] are typical metrics used to assess and  
83 compare anthropogenic and natural drivers of climate change. The aerosol RE  
84 represents the instantaneous radiative impact of atmospheric particles on the Earth's  
85 energy balance [*Heald et al., 2014*]. RF is calculated as the change of RE between  
86 two different periods, e.g., the pre-industrial and the present-day times [*Heald et al.,*  
87 *2014; Liu et al., 2007*], based on the aerosol and precursor gas emissions in the two  
88 periods [*Dentener et al., 2006; Lamarque et al., 2010*].

89 RF due to aerosol and radiation interactions (RFari) of biomass burning aerosols  
90 has been estimated since the IPCC second Assessment Report (AR2). Based on the  
91 Aerosol Comparisons between Observations and Models (AeroCom) Phase II  
92 simulations [*Bond et al., 2013; Myhre et al., 2013b*], RFari of biomass burning  
93 aerosols in the IPCC Fifth Assessment Report (AR5) is estimated to be  $0.0 \text{ W m}^{-2}$   
94 (ranging from  $-0.20$  to  $0.20 \text{ W m}^{-2}$ ), and RFari of biomass burning black carbon (BC)  
95 and primary organic matter (POM) are of the opposite sign (i.e.,  $0.10$  and  $-0.10 \text{ W m}^{-2}$ ,  
96 respectively).

97 There are also some studies that estimated the RE due to aerosol and radiation



198 interactions (RE<sub>ari</sub>) of fire aerosols by comparing the simulation with fire emissions  
199 against the simulation with no fire emissions. For example, using the NCAR  
200 Community Atmosphere Model version 4 (CAM4) with a bulk aerosol module, *Tosca*  
201 *et al.* [2013] reported that the top-of-atmosphere (TOA) RE<sub>ari</sub> from global biomass  
202 burning aerosols is  $0.18 \pm 0.10 \text{ W m}^{-2}$  averaged for the period of 1997-2009. *Ward et al.*  
203 [2012] estimated the RE<sub>ari</sub> from biomass burning aerosols in the pre-industrial (for  
204 the year 1850), present-day (for the year 2000), and future time periods (for the year  
205 2100), and found that the biomass burning aerosol RE<sub>ari</sub> for the year 2000 is  $0.13 \text{ W}$   
206  $\text{m}^{-2}$  and  $-0.27 \text{ W m}^{-2}$  in all-sky and clear-sky conditions, respectively.

207 RE due to aerosol and cloud interactions (RE<sub>aci</sub>) of biomass burning aerosols can  
208 be comparable in magnitude to or even stronger than the RE<sub>ari</sub> [*Liu et al.*, 2014].

209 With a global aerosol-climate model, the RE<sub>aci</sub> of biomass burning aerosols was  
210 estimated to range from  $-1.74$  to  $-1.00 \text{ W m}^{-2}$  for the year 2000 in *Ward et al.* [2012].

211 The semi-direct radiative effect of biomass burning aerosols is not independently  
212 assessed in IPCC reports. The magnitude was reported to be about  $7.0 \text{ W m}^{-2}$  in the  
213 Southern American biomass burning regions by examining the radiative flux  
214 difference with and without the biomass burning aerosol effect on clouds [*Liu*, 2005].

215 The RF or RE due to surface albedo changes (RF<sub>sac</sub> or RE<sub>sac</sub>) of BC from open  
216 fires and other sources has been estimated in previous studies. For biomass burning  
217 emissions with a strong (1998) and weak (2001) boreal fire year, RE of fire  
218 BC-in-snow was estimated to be  $0.011$  and  $0.006 \text{ W m}^{-2}$ , respectively [*Flanner et al.*,  
219 2007]. *Randerson et al.* [2006] reported that BC from a boreal forest fire deposited on

120 snow and sea ice introduced a global annual mean RE of  $8\pm 5$  W per  $\text{m}^2$  of burned area  
121 in the first year when the fire happened. A summary of BC-in-snow forcing/effect can  
122 be found in *Bond et al.* [2013]. They reported that the present-day RE of fire  
123 BC-in-snow ranges from 0.006 to  $0.02 \text{ W m}^{-2}$  based on previous studies [*Jacobson,*  
124 *2004; Rypdal et al., 2009; Skeie et al., 2011; Hansen et al., 2005; Flanner et al., 2007,*  
125 *2009; Koch et al., 2009*].

126 Biomass burning aerosols can have significant impacts on global and regional  
127 precipitation and atmospheric circulation. With the change of fire emissions from year  
128 1860 to 2000, *Jones et al.* [2007] found that biomass burning aerosols decrease the  
129 global near-surface air temperature by about  $0.25^\circ\text{C}$ , when considering the feedbacks  
130 of sea surface temperature (SST) in the model. As shown in *Tosca et al.* [2013], the  
131 direct and semi-direct effects of biomass burning aerosols reduce the precipitation  
132 near the equator and weaken the Hadley circulation. With a regional climate model,  
133 *Zhang et al.* [2009] found that biomass burning aerosols may warm and stabilize the  
134 lower troposphere and thus reinforce the dry season rainfall pattern in the Southern  
135 Amazonia. The absorption of shortwave radiation by biomass burning BC could  
136 increase the vertical stratification and inhibit both the cloud formation and  
137 precipitation [*Ackerman et al., 2000; Tosca et al., 2014*]. In contrast, biomass burning  
138 aerosols could invigorate the convective clouds [*Andreae et al., 2004a; Koren et al.,*  
139 *2005*] through suppressing warm rain processes in the convection, and enhance the  
140 latent heat release at higher levels [*Andreae and Rosenfeld, 2008*].

141 Although there have been many studies quantifying the RE of fire aerosols, a

142 further investigation is still needed, as the current estimations of fire aerosol RE are  
143 still associated with large uncertainties [e.g., *Myhre and Samset, 2015; Chakrabarty et*  
144 *al., 2014*]. The REs of co-emitted fire POM versus BC are even less clear. In this  
145 study, we estimate the present day (from year 2003 to 2011) open fire aerosol REs  
146 (including RE<sub>ari</sub>, RE<sub>aci</sub> and RE<sub>sac</sub>) using the NCAR Community Atmosphere Model  
147 version 5.3 (CAM5) with the four-mode version of the modal aerosol module  
148 (MAM4). We use two methods to calculate the RE<sub>ari</sub> of fire aerosols (total, BC-only,  
149 and POM-only). One method estimates the RE<sub>ari</sub> based on different model  
150 simulations [*Ghan, 2013*], and the other one calculates the RE<sub>ari</sub> directly through  
151 multiple diagnostic radiation calls in a single simulation. The spatial and seasonal  
152 characteristics of fire aerosol REs, and the impacts on the global precipitation and  
153 temperature are discussed.

154 Compared to earlier studies of fire aerosol REs [*Tosca et al., 2013; Ward et al.,*  
155 *2012*], a number of improvements are made in this study. First, a higher model  
156 horizontal resolution at 0.9° by 1.25° is used versus 1.9° by 2.5°. The higher  
157 resolution allows more efficient transport of aerosols from the sources to remote  
158 regions [*Ma et al., 2013; 2014*]. Model resolution has also been shown to be important  
159 for aerosol RE<sub>aci</sub> [*Ma et al., 2015*]. Second, the latest CAM5 model with MAM4 is  
160 used. MAM4 with an additional primary carbon mode explicitly treats the  
161 microphysical ageing of primary carbonaceous aerosols (POM/BC) in the atmosphere.  
162 MAM4 has higher BC and POM burdens over the earlier three-mode version of  
163 MAM (MAM3) in the remote regions by ~30% [*Liu et al., 2016*]. Third, daily instead

164 of monthly fire emissions are used, which allows the model to consider the effect of  
165 fast changes in the fire emission flux on local atmospheric conditions. It is expected  
166 that using the monthly mean emission flux the model can not consider the effect of  
167 extremely strong fires, thus it might underestimate the fire aerosol REs for such cases.  
168 Finally, a new methodology [Ghan, 2013] is used to more accurately diagnose the  
169 REs of fire aerosols. Central to this method is that the RE<sub>ari</sub> must be calculated in the  
170 presence of clouds (i.e., under the all-sky condition), and the RE<sub>aci</sub> be calculated  
171 under the condition of no aerosol effects on radiation. With the radiative forcing  
172 decomposition of this method, RE<sub>sac</sub> can also be quantified.

173 The paper is organized as follows. Section 2 introduces the model and  
174 experiments. Section 3 describes the methods to diagnose the fire aerosol REs.  
175 Section 4 presents the model results of fire aerosol REs, and impacts on global and  
176 regional surface temperature and precipitation. Conclusions and discussion are given  
177 in Section 5.

178

## 179 **2. Model, Experiment Design and Aerosol Radiative Effect Method**

### 180 **2.1 Model**

181 In our study, we use the Community Earth System Model (CESM) version 1.2,  
182 with the Community Atmosphere Model version 5.3 (CAM5.3) [Neale *et al.*, 2010]  
183 coupled with the Community Land Model version 4 (CLM4) [Oleson *et al.*, 2010].  
184 The SNOW, ICE, and Aerosol Radiative model (SNICAR) [Flanner and Zender, 2005]  
185 is turned on in the simulations to diagnose the biomass burning BC-in-snow effect.  
186 CAM5 includes several major updates in its physics parameterizations compared to

187 previous CAM versions. A two-moment stratiform cloud microphysics scheme is  
188 included in CAM5 to predict both the mass and number mixing ratios of cloud liquid  
189 and cloud ice [Morrison and Gettelman, 2008]. MAM4, which was updated from  
190 MAM3 [Liu *et al.*, 2012], includes aerosol mass and number mixing ratios in four  
191 lognormal modes: Aitken, accumulation, coarse, and primary carbon mode [Liu *et al.*,  
192 2016]. An additional primary carbon mode is included in MAM4 on the top of  
193 MAM3 to explicitly treat the microphysical ageing of primary carbonaceous aerosols  
194 (POM and BC) in the atmosphere. POM and BC in MAM4 are emitted in the primary  
195 carbon mode instead of directly in the accumulation mode as in MAM3. MAM4  
196 significantly increases the BC and POM concentrations in the remote regions (e.g.,  
197 over oceans and Arctic) due to reduced wet scavenging of POM and BC in the  
198 primary carbon mode with a lower hygroscopicity than that in the accumulation mode.  
199 The increase is relatively small in the land source regions [Liu *et al.*, 2016].

200

## 201 2.2 Experiment design

202 CAM5 was run with the finite volume dynamics core in a resolution of 0.9°  
203 latitude by 1.25° longitude and 30 vertical levels. The model was run for the time  
204 period of year 2003 to 2011 (i.e., for 9 years) with prescribed monthly SST and sea  
205 ice. The year 2003 was run twice and the first year simulation was used as a model  
206 spin-up. Global Fire Emissions Database version 3.1 (GFED 3.1) daily emissions  
207 [Giglio *et al.*, 2013] for BC, POM and sulfur dioxide (SO<sub>2</sub>) from 2003 to 2011 are  
208 prescribed, and the vertical distribution of fire emissions is based on the AeroCom

209 protocol [*Dentener et al.*, 2006]. Anthropogenic aerosol and precursor gas emissions  
210 are from the IPCC AR5 dataset [*Lamarque et al.*, 2010]. We performed our control  
211 experiment (FIRE) with the GFED fire emissions turned on and a sensitivity  
212 experiment (NOFIRE) with the fire emissions turned off. Differences between FIRE  
213 and NOFIRE experiments are used to calculate the REs and atmospheric effects of  
214 biomass burning aerosols on temperature and precipitation. Two additional  
215 experiments (NOFIREBC and NOFIREPOM) were performed with fire BC and POM  
216 emissions turned off, respectively. Differences between the control (FIRE) and these  
217 two experiments represent the contribution from biomass burning BC and POM,  
218 respectively. Other forcings (e.g., SST, greenhouse gases) of all these experiments are  
219 kept the same. We performed ten ensemble members for each of these experiments.  
220 Furthermore, we performed the other experiment (FIRE\_BBFFBF) using the modified  
221 CAM5 model that separately predicts the BC and POM from biomass burning (BB),  
222 fossil fuel (FF) and biofuel (BF) sources, while other model features are kept the same  
223 as the FIRE experiment. A summary of all the experiments in this study can be found  
224 in Table 1.

225

### 226 2.3 Methods of calculating fire aerosol radiative effects

227 The REs of all fire aerosols, fire BC, and fire POM are calculated from the  
228 differences of TOA shortwave fluxes ( $\Delta F$ ) between the FIRE experiment and the  
229 three other experiments (NOFIRE, NOFIREBC and NOFIREPOM), respectively. All  
230 the atmospheric variables (including temperature, precipitation, and circulation) are

231 allowed to adjust in the experiments. However, with SST and sea ice prescribed in  
 232 these experiments, only the rapid adjustments are taken into account. Thus the  
 233 *effective* radiative effects are actually calculated in this study.

$$234 \quad \Delta F_{\text{fire aero}} = F_{\text{fire}} - F_{\text{nofire}} \quad (1)$$

$$235 \quad \Delta F_{\text{fire bc}} = F_{\text{fire}} - F_{\text{nofirebc}} \quad (2)$$

$$236 \quad \Delta F_{\text{fire pom}} = F_{\text{fire}} - F_{\text{nofirepom}} \quad (3)$$

237 The total TOA shortwave flux change can be broken into the REari, REaci, and  
 238 RESac. The aerosol REaci results from both the aerosol effect on clouds via acting as  
 239 CCN and the aerosol semi-direct effect on clouds via affecting the atmospheric states  
 240 due to absorbing aerosols. We adopt the method of *Ghan* [2013] to separate the REari,  
 241 REaci, and RESac from the total effects of all fire aerosols, fire BC and fire POM,  
 242 respectively. The method is summarized as follows.  $F_{\text{clean}}$  is the radiative flux at TOA  
 243 calculated from a *diagnostic radiation call* in the same control simulations, but  
 244 neglecting the scattering and absorption of solar radiation by aerosols.  $F_{\text{clean,clear}}$  is the  
 245 clear-sky radiative flux at TOA calculated from the same *diagnostic radiation call*,  
 246 but neglecting scattering and absorption by both clouds and aerosols.

$$247 \quad \Delta F = \underbrace{\Delta(F - F_{\text{clean}})}_{(\text{REari})} + \underbrace{\Delta(F_{\text{clean}} - F_{\text{clean,clear}})}_{(\text{REaci})} + \underbrace{\Delta F_{\text{clean,clear}}}_{(\text{RESac})} \quad (4)$$

249 In the method above, REaci includes both aerosol indirect and semi-direct effects.  
 250 The fire BC has a much weaker indirect effect due to its lower mass burden and lower  
 251 hygroscopicity compared to fire POM [*Koch et al.*, 2011]. Thus the fire aerosol  
 252 semi-direct effect can be approximately represented by the REaci of fire BC. The fire

253 aerosol indirect effect can be estimated as the difference of fire aerosol RE<sub>aci</sub> and  
254 semi-direct effect. With the sea ice prescribed in these experiments, the radiative  
255 effect of fire aerosols on sea ice albedo is not considered in RE<sub>sac</sub>.

256 We undertake another method to estimate the fire aerosol RE<sub>ari</sub> from the  
257 experiment (FIRE\_BBFFBF). With explicit predictions of fire POM and fire BC in  
258 FIRE\_BBFFBF, the RE<sub>ari</sub> of fire BC and fire POM are estimated by two diagnostic  
259 radiation calls, each time neglecting the scattering and absorption of solar radiation of  
260 fire BC and fire POM, respectively. This more direct method is named as BBFFBF,  
261 and the RE<sub>ari</sub> of fire BC and fire POM will be compared with those from the method  
262 of *Ghan* [2013]. The fire BC-in-snow effect is calculated from SNICAR, and  
263 compared with the RE<sub>sac</sub> estimated from *Ghan* [2013].

264

### 265 **3. Results**

#### 266 3.1 Simulation of biomass burning aerosols

267 The biomass burning BC and POM from forest, grass and agriculture fires are  
268 significant contributors to the total BC and POM emissions. Figure 1 shows the  
269 seasonal variation of GFED fire emissions (including forest, grass and agriculture  
270 fires) in the global, tropical (25°S to 25°N), and Arctic (60°N to 90°N) regions.  
271 Global fire emission is the largest during the boreal summer as well as in the boreal  
272 autumn (September/October), when it is the fire season in the tropical regions of the  
273 Southern Hemisphere (SH). The tropical fire emission contributes the most to the  
274 annual global fire emission (80% for BC and 85% for OC, respectively), compared to



275 other regions. Arctic is the other important fire region, where the emission maximum  
276 is found during the boreal summer. In the boreal summer, the OC emission in the  
277 Arctic regions is about 50% of that in the tropical region. The BC emission in the  
278 Arctic is much smaller than that of the tropical regions even in the boreal summer fire  
279 season. The dominant fire type in the SH tropics is deforestation, savanna and  
280 grassland fires, while that in the Arctic is the forest fires. The OC to BC ratio (OC/BC)  
281 of forest fires is almost three times higher than that of deforestation, savanna and  
282 grassland fires [*van der Werf et al.*, 2010].

283 Figure S1 in the supplemental materials shows the latitudinal and longitudinal  
284 distributions of vertically integrated concentrations (column burdens) of BC and POM  
285 from BB, FF, and BF sources based on the FIRE\_BBFFBF experiment. The BC and  
286 POM from BB source are mainly distributed in the tropical and sub-tropical regions  
287 (southern Africa, South America and Southeast Asia) and in the mid- to high latitudes  
288 (North of 45°N) of the Northern Hemisphere (NH) (Northeast Asia, Alaska and  
289 Canada). The largest column burdens of biomass burning aerosols are located in  
290 southern Africa and adjacent oceanic areas (1.5 and 20 mg m<sup>-2</sup> for BC and POM,  
291 respectively). The biomass burning aerosols are important aerosol species in the  
292 Arctic regions, and contribute up to 53% and 86% to the total burden of BC and POM  
293 in the Arctic (from 60° N to 90°N), respectively. In comparison, the maximum  
294 column burdens of fossil fuel BC and POM are found in East Asia, South Asia,  
295 Western Europe and North America. The maximum column burdens of biofuel BC  
296 and POM occur in East Asia, South Asia and Central Africa. The biofuel and fossil

297 fuel sources are dominant contributors to BC and POM in East Asia and South Asia.  
298 In other regions of the world, biomass burning is the primary source of BC and POM.  
299 Globally, the biomass burning contributes 41% and 70% to the total burdens of BC  
300 and POM, respectively. Biomass burning can also emit SO<sub>2</sub>. However, it only  
301 contributes ~3% to the total global sulfate burden (figure not shown), so only  
302 radiative effects of biomass burning POM and BC are discussed in this study.

303 The simulated aerosol optical depth (AOD) and single scattering albedo (SSA)  
304 (including aerosols from all sources) are validated with observations from the  
305 AErosol RObotic NETwork (AERONET, <http://aeronet.gsfc.nasa.gov>) at sites  
306 significantly affected by biomass burning activity in southern Africa, South America  
307 and the Arctic regions, as shown in Figures 2 and 3 (see Figure S2 in the  
308 supplemental materials for the site locations). The AERONET AOD and SSA data are  
309 averaged for the years from 2003 to 2011 to match the simulation period, although  
310 there are missing AERONET data for some periods. We note that *Tosca et al.* [2013]  
311 and *Ward et al.* [2012] applied scaling factors (from 1 to 3 varying by regions) to fire  
312 emissions to improve modeled AOD magnitudes, whereas here we do not apply any  
313 such scaling. In southern Africa, modeled monthly AOD agrees with observations  
314 within a factor of 2 for the three sites (Figure 2a-2c). The underestimation of AOD is  
315 found in the tropical site (Mongu) (Figure 2a) during the boreal autumn (the fire  
316 season). The simulated AOD in the two other sites (Skukuza and Ascension Island) is  
317 generally consistent with observations in both the magnitude and seasonal trend. The  
318 simulated SSA in southern Africa ranges between 0.75 and 0.95 and generally

319 matches the observed SSA magnitude and seasonal cycle in the two land sites (Mongu  
320 and Skukuza) (Figure 3a-3b). However, an overestimation of SSA is found in the  
321 oceanic site (Ascension Island) (Figure 3c). The reason for this overestimation of SSA  
322 and thus the underestimation of absorption AOD (AAOD) is unclear and could be due  
323 to that the model has not treated the absorption enhancement of aged fire BC during  
324 its transport.

325 The simulated AOD in South America is generally consistent with observations  
326 within a factor of 2 (Figure 2d-2f). The seasonal variation of simulated AOD  
327 generally matches the observations. The underestimation of AOD in Alta Floresta and  
328 Cuiaba-Miranda is most obvious in September and October (the fire season), which  
329 may be attributed to the underestimation of fire emissions. However, the modeled  
330 AOD is higher than observations before the fire season for Alta Floresta and Rio  
331 Branco, which could be due to the overestimation of fire emission in this period. The  
332 simulated SSA in South America ranges mostly between 0.87–0.95 and matches the  
333 observations reasonably well (Figure 3d-3f). The modeled SSA is too low during the  
334 fire season and exhibits too strong a seasonality. It implies that the model  
335 underestimation of scattering aerosols (e.g., POM) may be more severe than that of  
336 BC during the fire season.

337 In the Arctic, small AOD (less than 0.3) and large SSA (larger than 0.9) are  
338 observed for the three sites. The observed large SSA in the fire season (boreal  
339 summer) is consistent with the high OC/BC ratio of fire emissions in the Arctic  
340 (Figure 1). The model significantly underestimates the observed AOD in the Arctic in

341 both fire and non-fire seasons. The underestimation of AOD can be due to (1) the  
342 underestimation of fire emissions in the NH high latitudes [e.g., *Stohl et al.*, 2013]  
343 and/or fossil fuel emissions in Asia [e.g., *Cohen and Wang*, 2014], (2) the excessive  
344 scavenging of aerosols during their transport from the NH mid-latitude industrial  
345 regions by liquid-phase clouds [*Wang et al.*, 2013a], and (3) the coarse horizontal  
346 resolution ( $\sim 100$  km) of the model [*Ma et al.*, 2014]. Although MAM4 increases the  
347 column burdens of POM and BC by up to 40 % in many remote regions compared to  
348 MAM3, it still underestimates the surface BC concentrations in the Arctic [*Liu et al.*,  
349 2016]. The modeled SSA in the Arctic is lower than observations, which implies that  
350 the simulation of AAOD is better than that of AOD and the underestimation of  
351 non-absorbing aerosols (e.g., sulfate and POM) in the Arctic may be more severe than  
352 that of BC.

353

### 354 3.2 Radiative effect due to aerosol-radiation interactions

355 The annual mean RE<sub>ari</sub> of all fire aerosols (including BC, POM and sulfate)  
356 estimated with the method of BBFFBF and with the method of *Ghan* [2013] is shown  
357 in Figure 4a-4b. The fire sulfate is not included in the calculation of RE<sub>ari</sub> of all fire  
358 aerosols with the method of BBFFBF. Its effect is minor since the global annual mean  
359 burden of fire sulfate ( $0.09 \text{ mg m}^{-2}$ ) is much smaller than that of fire POM ( $1.25 \text{ mg}$   
360  $\text{m}^{-2}$ ), both of which are light-scattering. The statistical significance of RE<sub>ari</sub> estimated  
361 with the *Ghan* [2013] method over the interannual variability and ensemble member  
362 diversity is shown in Figure 4 (and also later figures). The RE<sub>ari</sub> of all fire aerosols

363 from the two methods agree with each other very well. Thus, we will report the REari  
364 of all fire aerosols with the *Ghan* [2013] method below. The global annual mean  
365 REari of all fire aerosols is positive ( $0.16 \pm 0.01 \text{ W m}^{-2}$ ), which indicates a warming  
366 effect from all fire aerosols. The REari is positive on the globe except in some land  
367 areas (e.g., southern Africa, South America, Great Lakes, North Canada, and East  
368 Siberia). The maximum positive REari is located in ocean areas west of southern  
369 Africa ( $\sim 5.0 \text{ W m}^{-2}$ ) and South America ( $\sim 1.5 \text{ W m}^{-2}$ ). Positive REari up to  $1 \text{ W m}^{-2}$  is  
370 found in the Arctic ( $60^\circ\text{N}$  to  $90^\circ\text{N}$ ). The different signs of REari between land and  
371 ocean areas of southern Africa and South America result from the differences in cloud  
372 fraction and cloud liquid water path (LWP) between land and ocean regions. In the  
373 fire season (August-September-October) of the SH tropical regions, cloud fraction  
374 and cloud LWP over the land areas (10% and  $20 \text{ g m}^{-2}$ , respectively) are much smaller  
375 than those over the adjacent ocean areas (70% and  $70 \text{ g m}^{-2}$ , respectively). The  
376 biomass burning aerosols are transported above the low-level stratocumulus clouds,  
377 and when biomass burning BC resides above clouds, its absorption of solar radiation  
378 is significantly enhanced due to the reflection of solar radiation by underlying clouds  
379 [*Abel et al.*, 2005; *Zhang et al.*, 2016].

380 A comparison of modeled REari in the boreal autumn  
381 (September-October-November) over the South Atlantic Ocean with satellite  
382 observations is shown in Figure 5. The observed above-cloud aerosol REari is  
383 calculated with the method of *Zhang et al.* [2014] using the Aqua/MODIS and  
384 Terra/MODIS products, respectively. The observed above-cloud aerosol REari over

385 southeastern Atlantic Ocean is  $3\text{-}12 \text{ W m}^{-2}$ , with higher values near the coasts. The  
386 simulated REari agrees better with Aqua/MODIS observed REari than with  
387 Terra/MODIS in both the magnitude and spatial pattern. REari estimated from  
388 Terra/MODIS (morning time) is stronger than the one estimated from Aqua/MODIS  
389 (afternoon time) due to the larger amount of underlying clouds in the morning [*Min*  
390 *and Zhang*, 2014]. Over South America during the fire season (August to September),  
391 the clear-sky fire aerosol REari is estimated to be  $-5.2 \text{ W m}^{-2}$  by *Sena and Artaxo*  
392 [2015], which is larger than our model result ( $-2.1 \text{ W m}^{-2}$ ). This is consistent with the  
393 underestimation of modeled AOD in South America compared to the AERONET data  
394 (Figure 2).

395 The seasonal variation of REari of all fire aerosols with the *Ghan* [2013] method  
396 is shown in the supplemental Figure S3. The REari has a maximum ( $1.13 \text{ W m}^{-2}$ ) in  
397 the boreal summer (June-July-August, JJA) over the Arctic regions, partially due to  
398 the low solar zenith angles there. The maximum positive REari in the tropical regions  
399 occurs in the boreal summer and autumn (September, October and November, SON)  
400 during the fire season of southern Africa and South America. The REari reaches a  
401 positive maximum in Southeast Asia during the fire season in March, April and May  
402 (MAM).

403 The REari of fire BC is shown in Figure 4c-4d. The fire BC REari calculated  
404 from the two methods are similar in magnitudes and spatial patterns, and there is  
405 much less noise with the BBFFBF method. The global annual mean fire BC REari is  
406 about  $0.25 \pm 0.01 \text{ W m}^{-2}$  and positive over the globe (the regions with negative values

407 in Figure 4d are in general not statistically significant). Unlike all fire aerosols, fire  
408 BC generates a positive forcing in the land regions of southern Africa and South  
409 America, and the amplification effect of low-level clouds on fire BC positive forcing  
410 can be clearly seen in southern Africa and adjacent Atlantic Ocean.

411 The global annual mean RE<sub>ari</sub> of fire POM from the two methods somewhat  
412 differs from each other (Figure 4e-4f). The BBFFBF method gives a small negative  
413 value ( $-0.05 \text{ W m}^{-2}$ ), while the *Ghan* [2013] method shows a small positive value  
414 ( $0.04 \pm 0.01 \text{ W m}^{-2}$ ). The difference is mainly in the Arctic regions where the positive  
415 forcing from *Ghan* [2013] is larger than that from the BBFFBF method. This is  
416 because the removal of fire POM emissions in the NOFIREPOM experiment affects  
417 the properties of aerosol particles within which co-emitted fire BC is internally mixed  
418 with fire POM, causing a decrease of BC burden in the Arctic (by  $\sim 0.05 \text{ mg m}^{-2}$ )  
419 compared to the FIRE experiment. Thus, one should be careful in using the *Ghan*  
420 [2013] method to diagnose the radiative forcing of a single component within  
421 co-emitted aerosols. The RE<sub>ari</sub> of fire POM is negative in most of the globe. However,  
422 positive forcing can be found over oceanic regions west of southern Africa and South  
423 America, North Pacific Ocean and the Polar regions where large amount of low-level  
424 clouds, sea ice or land ice exist. The multiple scatterings between the above-cloud fire  
425 POM and low-level clouds or between the fire POM and the Earth's bright surface  
426 with high albedos could reduce the amount of solar radiation reflected by these  
427 low-level clouds and bright surface in the case without the fire POM [*Zhang et al.*,  
428 2016]. With the BBFFBF method the sum of RE<sub>ari</sub> from fire POM and fire BC (i.e.,

429  $0.20 \text{ W m}^{-2}$ ) is larger than that of all fire aerosols ( $0.15 \text{ W m}^{-2}$ ). It reflects the  
430 nonlinear interactions among different aerosol components [Ghan et al., 2012]. The  
431 nonlinearity is stronger with the Ghan [2013] method.

432

### 433 3.3 Radiative effect due to aerosol-cloud interactions

434 The annual mean REaci due to all fire aerosols, fire BC, and fire POM are shown  
435 in Figure 6. The REaci diagnosed with the Ghan [2013] method includes both aerosol  
436 indirect and semi-direct effects. The fire aerosol semi-direct effect (to be discussed  
437 below) is much smaller ( $-0.04 \pm 0.03 \text{ W m}^{-2}$  on the global mean) than the indirect  
438 effect, and the REaci is mostly from the fire aerosol indirect effect. The global annual  
439 mean REaci of all fire aerosols is  $-0.70 \pm 0.05 \text{ W m}^{-2}$  (Figure 6a). In the tropical  
440 regions, the strong negative REaci is located in the adjacent ocean areas of southern  
441 Africa, South America and Australia, with the maximum REaci of  $-8.0 \text{ W m}^{-2}$  over  
442 the South Atlantic Ocean. The strong negative REaci also occurs in the Arctic ( $60^\circ\text{N}$   
443 to  $90^\circ\text{N}$ ). The REaci in East Siberia, Alaska and Canada is as large as  $-6.0 \text{ W m}^{-2}$ .

444 The fire BC has a weak indirect effect by acting as CCN, but can reduce the cloud  
445 amount through its semi-direct effect. The REaci of fire BC (Figure 6b) can  
446 approximate the fire BC semi-direct effect with a small global annual mean value of  
447  $-0.04 \pm 0.03 \text{ W m}^{-2}$ . However, stronger positive effect can be found in the western  
448 Pacific ( $3.0 \text{ W m}^{-2}$ ) and Arctic regions ( $1.0 \text{ W m}^{-2}$ ). The global annual mean REaci of  
449 fire POM is  $-0.59 \pm 0.03 \text{ W m}^{-2}$  (Figure 6c), and dominates the cloud effect of all fire  
450 aerosols. The sum of REaci from fire BC and POM ( $-0.62 \pm 0.03 \text{ W m}^{-2}$ ) is smaller



451 than that of all fire aerosols ( $-0.70 \pm 0.05 \text{ W m}^{-2}$ ) due to the non-linear interactions of  
452 fire BC and fire POM [*Jiang et al.*, 2013] as well as the negative REaci of fire sulfate.

453 The seasonal variation of all fire aerosol REaci is shown in Figure 7. The  
454 maximum of fire aerosol REaci is in the boreal summer (i.e., the fire season in NH)  
455 located in the NH high latitudes ( $60^\circ\text{N}$  to  $90^\circ\text{N}$ ). The largest summer REaci is found  
456 in the land areas and is as large as  $-15 \text{ W m}^{-2}$ . The fire aerosol REaci in the tropical  
457 regions is most significant in the boreal summer (up to  $-15 \text{ W m}^{-2}$ ) and autumn (up to  
458  $-10 \text{ W m}^{-2}$ ) over the ocean areas. The different spatial distributions of fire aerosol  
459 REaci in the NH high latitudes and in the tropics result from the difference in cloud  
460 distributions between the two regions. During the fire season the cloud LWP over the  
461 land areas in the NH mid- and high latitudes is three times larger than that over the  
462 ocean areas in the tropics. Larger cloud LWP favors the stronger REaci, because the  
463 larger LWP associated with the warm cloud and rain processes favors the aerosol  
464 indirect effect via slowing down the autoconversion of cloud water to rain [*Ghan et*  
465 *al.*, 2012; *Jiang et al.*, 2015]. Meanwhile, in the NH high latitudes, the lower solar  
466 zenith angle in the boreal summer favors the stronger REaci. Like the fire aerosol  
467 REari, the smallest fire aerosol REaci occurs in the boreal spring.

468 Seasonal variations of zonal mean fire aerosol REari, REaci, cloud LWP,  
469 low-level (from surface to 750 hPa) cloud amount, and vertically-integrated (burden)  
470 concentrations of fire POM and fire BC are shown in Figure 8. The seasonal variation  
471 of fire BC and fire POM burdens is largest in the SH low latitudes (from  $30^\circ\text{S}$  to  $0^\circ\text{N}$ )  
472 and NH mid- and high latitudes ( $50^\circ\text{N}$  to  $90^\circ\text{N}$ ). Distinct features of these two areas

473 can also be noticed that the maximum fire BC burden in NH ( $0.3 \text{ mg m}^{-2}$ ) is much  
474 lower than that in SH ( $0.8 \text{ mg m}^{-2}$ ), while the maximum POM burdens in these two  
475 areas are comparable. Interestingly, the REari is larger in the boreal summer in NH  
476 than that in the boreal autumn in SH, although the fire BC burden is much lower in  
477 the NH summer. It is mainly due to the larger amount of low clouds in the NH high  
478 latitudes, which enhances the absorption of fire BC. The maximum REari in the NH  
479 summer is found near the North Pole ( $70^\circ\text{N}$  to  $90^\circ\text{N}$ ), and not around  $60^\circ\text{N}$  where  
480 the fire aerosol burden is highest. The REaci of fire aerosols is about 3 times larger in  
481 the boreal summer in NH than that in the boreal autumn in SH, although the burden of  
482 fire POM in NH is comparable to that in SH. The larger cloud LWP in the NH  
483 summer around  $40\text{-}70^\circ\text{N}$  favors the stronger REaci there.

484

#### 485 3.4 Surface albedo effect

486 Here we compare the modeled BC-in-snow (BCS) concentrations with  
487 observation data collected from multiple field campaigns over the Arctic [*Doherty et*  
488 *al.*, 2010] and Northern China [*Wang et al.*, 2013b; *Qian et al.*, 2014]. Figure 9a  
489 shows the simulated (from FIRE and NOFIRE experiments) and observed BCS  
490 concentrations as a function of latitude. The range of observed BCS concentrations is  
491 between  $1$  and  $200 \text{ ng g}^{-1}$  in the Arctic and between  $50$  and  $2000 \text{ ng g}^{-1}$  in Northern  
492 China, respectively. Both FIRE and NOFIRE experiments capture the meridional  
493 gradient in BCS concentrations between the mid-latitudes (Northern China) and high  
494 latitudes (Arctic). The mean and median concentrations of BCS are both

495 overestimated in Northern China, implying the high biases from the anthropogenic  
496 emissions and/or model physics (Figure 9b). The mean and median BCS  
497 concentrations from the FIRE experiment agree slightly better with observations than  
498 those from the NOFIRE experiment in the Arctic (Figure 9b). This suggests that fire  
499 emissions are important for BCS concentrations in the Arctic.

500 The annual mean RE<sub>sac</sub> of all fire aerosols estimated with *Ghan* [2013] and the  
501 fire BCS effect diagnosed from SNICAR are shown in Figure 10a. We note that the  
502 radiative effect due to BC deposition on sea ice is not considered since sea ice is  
503 prescribed in the simulations. The global annual mean RE<sub>sac</sub> ( $0.03 \pm 0.10 \text{ W m}^{-2}$ ) is  
504 much smaller compared to the RE<sub>ari</sub> and RE<sub>aci</sub>. The RE<sub>sac</sub> over land is maximum in  
505 spring ( $0.12 \pm 0.27 \text{ W m}^{-2}$ ) and winter ( $0.06 \pm 0.16 \text{ W m}^{-2}$ ). The RE<sub>sac</sub> over land in  
506 summer and autumn is very small (less than  $0.01 \text{ W m}^{-2}$ ). We note that the mean  
507 RE<sub>sac</sub> calculated with *Ghan* [2013] is much smaller than the standard deviation  
508 resulted from the internal variability.

509 The annual mean fire BCS effect calculated from SNICAR is shown in Figure  
510 10b and 10c. The spatial distribution of the fire BCS effect is similar to the fire RE<sub>sac</sub>,  
511 implying that the fire RE<sub>sac</sub> has a significant contribution from the fire BCS effect.  
512 Averaged when only snow is present, the fire BCS effect is larger ( $0.048 \text{ W m}^{-2}$ ). The  
513 global mean fire BCS effect (with the presence of snow) can be as large as  $0.06 \text{ W m}^{-2}$   
514 in spring. The maximum fire BCS effect (up to  $1 \text{ W m}^{-2}$ ) is located in Greenland and  
515 the very northern reaches of Canada, while that in the other Arctic regions and North  
516 China is smaller.

517 The positive RE<sub>sac</sub> in Siberia, North America and Canada can be a result of BCS  
518 effect. However, the RE<sub>sac</sub> in these regions is larger than the BCS effect especially in  
519 spring. The snow melting and snow depth change due to the BCS warming may  
520 induce a larger positive RE<sub>sac</sub> than the albedo change due to BCS itself. The negative  
521 RE<sub>sac</sub> over land can be a result of atmospheric feedbacks caused by fire aerosols  
522 [*Ghan*, 2013].

523

### 524 3.5 Fire aerosol effects on shortwave radiation, global temperature and precipitation

525 Here, we show the annual mean net shortwave flux change at TOA (i.e., total  
526 radiative effect), in the atmosphere and at surface, and changes in surface air  
527 temperature, convective and large-scale precipitation due to all fire aerosols in Figure  
528 11 and Table 2. The global mean net shortwave flux change at TOA due to all fire  
529 aerosols is  $-0.55 \pm 0.07 \text{ W m}^{-2}$ , which indicates that fire aerosols lead to the reduction  
530 of shortwave flux into the Earth's system. The zonal mean TOA shortwave flux  
531 reduction in the Arctic regions ( $-1.35 \pm 1.03 \text{ W m}^{-2}$ ) is much larger than that in the  
532 tropical regions ( $-0.66 \pm 0.09 \text{ W m}^{-2}$ ). The cooling at TOA is mostly from fire aerosol  
533 RE<sub>aci</sub>. The maximum negative RE is located in the land areas of the Arctic and ocean  
534 areas of the tropics. Although the global mean total radiative effect is negative,  
535 positive effect is found in some land areas (e.g., Africa, Greenland).

536 The shortwave atmospheric absorption change in the tropical regions is larger  
537 than that in the Arctic regions. It is because BC burden in the tropics ( $0.17 \text{ mg m}^{-2}$ ) is  
538 larger than that in the Arctic ( $0.09 \text{ mg m}^{-2}$ ). Strong absorption ( $\sim 8 \text{ W m}^{-2}$ ) in the

539 atmosphere is found in the land areas of southern Africa and South America and in  
540 the Southeast Atlantic. The surface shortwave flux change in the Arctic is mostly  
541 from the TOA shortwave flux reduction due to the fire aerosol REaci, while the  
542 surface shortwave flux change in the tropics is mostly due to the fire BC absorption in  
543 the atmosphere.

544 The fire aerosols lead to the reduction of the global mean surface air temperature  
545 ( $T_s$ ) by  $0.03 \pm 0.03$  K, consistent with the reduction of shortwave fluxes at TOA and at  
546 surface. The largest surface cooling is found in the Arctic and tropical regions by up  
547 to 0.6 K. The cooling of the Arctic is related to the strong fire aerosol REaci, while  
548 the cooling in the tropics is mainly from the surface shortwave flux reduction due to  
549 the fire BC absorption. The  $T_s$  change in the ocean areas is very small since the SST is  
550 prescribed in our simulations.

551 The global mean total precipitation is reduced by  $0.010 \pm 0.002$  mm day<sup>-1</sup> due to  
552 all fire aerosols (Table 2). Unlike the  $T_s$  change, the precipitation reduction in the  
553 tropics ( $0.016 \pm 0.01$  mm day<sup>-1</sup>) is much larger than that in the Arctic ( $0.001 \pm 0.02$   
554 mm day<sup>-1</sup>, not statistically significant). The reduction in the tropics is mainly from the  
555 large-scale precipitation decrease ( $0.015 \pm 0.003$  mm day<sup>-1</sup>). The net decrease in the  
556 convective precipitation is very small in the tropics ( $0.001 \pm 0.009$  mm day<sup>-1</sup>, not  
557 statistically significant), as the convective precipitation is significantly decreased near  
558 the equator and increased in the regions away from the equator, partly consistent with  
559 the results of *Tosca et al.* [2013]. The precipitation reduction in southern Africa is  
560 consistent with the recent findings of *Hodnebrog et al.* [2016]. The shortwave flux

561 reduction at surface leads to a stabilization of the atmospheric boundary layer and a  
562 suppression of the convection near the equator. The strong atmospheric absorption by  
563 fire BC leads to the reduction of low-level clouds and large-scale precipitation in the  
564 tropics. Both effects lead to a significant reduction of total precipitation near the  
565 equator. The precipitation decrease in the NH high latitudes is mainly from the  
566 reduction of convective precipitation. We note that the temperature and (especially)  
567 precipitation changes reported here do not represent the complete impact of fire  
568 aerosols, since the SSTs are fixed in our simulations. Fully-coupled atmosphere and  
569 ocean models will be used to further investigate the impact of fire aerosols.

570 Figure 12 shows the changes of  $T_s$ , total precipitation, cloud LWP, and low-level  
571 cloud cover in the summer due to all fire aerosols. The  $T_s$  is reduced by more than 1 K  
572 in most of land areas around 60°N. The maximum cooling (larger than 1.5 K) is found  
573 in East Siberia, Alaska and Canada. A decrease of total precipitation (by about 0.2  
574 mm day<sup>-1</sup>) is found in these regions. Accompanying the surface cooling and  
575 precipitation reduction, a significant increase of cloud LWP and low-level cloud cover  
576 is found there. This is a result of the indirect effect of fire aerosols in the land areas of  
577 the Arctic (60°N to 90°N). The fire POM leads to the reduction of cloud droplet  
578 effective radius and the increase of cloud droplet number concentration, consistent  
579 with observed fire effects on clouds in Canada and the United States [*Peng et al.*,  
580 2002].

581

#### 582 **4. Discussion and Conclusions**

583        Although many studies have been conducted on the fire aerosol RE and RF [e.g.,  
584        *Bond et al.*, 2013; *Myhre et al.*, 2013b; *Ward et al.*, 2012; *Tosca et al.*, 2013], the  
585        current estimations are still associated with large uncertainties. In this study, the fire  
586        aerosol RE (including RE<sub>ari</sub>, RE<sub>aci</sub> and RE<sub>sac</sub>) is calculated based on a new method  
587        from *Ghan* [2013]. In addition, the fire aerosol RE<sub>ari</sub> and fire BC-in-snow effect are  
588        diagnosed from an experiment of CESM which tracks the open fire BC and POM  
589        separately from fossil fuel and biofuel sources and compared with the estimates from  
590        the *Ghan* [2013] method.

591        The BC and POM burdens from open fires are largest in the tropical regions  
592        (southern Africa, South America and Southeast Asia) and in the NH mid- to high  
593        latitudes (North of 45°N) (Northeast Asia, Alaska and Canada). Fire aerosols  
594        contribute 41% and 70% to the global burden of BC and POM, respectively. When  
595        comparing with the AERONET AOD and SSA data, modeled monthly AOD agrees  
596        with observations within a factor of 2 for most of the southern African and South  
597        American sites. The model underestimation of AOD is found in the South American  
598        sites near fire source regions, which is most obvious in the fire season (September and  
599        October). The model underestimates the observed AOD in the Arctic regions in both  
600        fire and non-fire seasons. The modeled SSA in southern Africa and South America is  
601        generally in agreement with observations, while the modeled SSA in the Arctic is  
602        lower.

603        The annual mean RE<sub>ari</sub> of all fire aerosols is  $0.16 \pm 0.01 \text{ W m}^{-2}$  and positive over  
604        most areas except in some land areas (e.g., southern Africa, North Canada, and East

605 Siberia). The annual maximum RE<sub>ari</sub> is found in the oceanic areas west of southern  
606 Africa ( $5 \text{ W m}^{-2}$ ) and South America ( $1.5 \text{ W m}^{-2}$ ). The positive RE<sub>ari</sub> over the land  
607 regions of southern Africa and South America is smaller, although the fire aerosol  
608 burdens are higher. The annual zonal mean RE<sub>ari</sub> in the Arctic regions can reach  $0.43$   
609  $\pm 0.028 \text{ W m}^{-2}$ , and is larger than that in the tropical regions ( $0.17 \pm 0.017 \text{ W m}^{-2}$ ),  
610 although the fire aerosol burden is higher in the tropics. The annual mean RE<sub>ari</sub> of  
611 fire BC is about  $0.25 \pm 0.01 \text{ W m}^{-2}$  and positive over the globe. Fire POM induces a  
612 weak negative RE<sub>ari</sub> globally ( $-0.05 \text{ W m}^{-2}$ ) with the BBFFBF method and a small  
613 positive value ( $0.04 \pm 0.01 \text{ W m}^{-2}$ ) with the *Ghan* [2013] method. The positive RE<sub>ari</sub>  
614 of fire POM is found over oceanic areas west of southern Africa and South America,  
615 North Pacific, and polar regions where the low-level cloud coverage is large or the  
616 surface albedo is higher.

617 The global annual mean RE<sub>aci</sub> of all fire aerosols is  $-0.70 \pm 0.05 \text{ W m}^{-2}$  and the  
618 maximum effect is located in the ocean areas west of southern Africa and South  
619 America and land areas of the NH high latitudes. The maximum fire aerosol RE<sub>aci</sub>  
620 occurs in the NH high latitudes in the boreal summer, which results from the large  
621 cloud LWP over the land areas and the low solar zenith angle. Associated with the  
622 strong indirect effects of fire aerosols in the Arctic summer, significant surface  
623 cooling, precipitation reduction, and low-level cloud cover increase are found in these  
624 regions.

625 Modeled BCS concentrations from the FIRE experiment are evaluated against  
626 observations in Northern China and in the Arctic, and generally agree with the



627 observations for the mean and median values in the Arctic regions. The high bias of  
628 modeled BCS concentrations in Northern China may not result from the fire BC  
629 because differences in BCS concentrations between FIRE and NOFIRE experiments  
630 are very small in North China. The global annual mean RE<sub>sac</sub> is  $0.03 \pm 0.10 \text{ W m}^{-2}$   
631 (statistically insignificant) with the maximum effect in spring ( $0.12 \text{ W m}^{-2}$ ). The  
632 RE<sub>sac</sub> is mainly due to the effect of fire BC deposit on snow ( $0.02 \text{ W m}^{-2}$ ) diagnosed  
633 from SNICAR with the maximum effect as large as  $0.06 \text{ W m}^{-2}$  (when snow is present)  
634 in spring.

635 The fire aerosols reduce the global mean surface air temperature ( $T_s$ ) by  $0.03 \pm$   
636  $0.03 \text{ K}$  and precipitation by  $0.01 \pm 0.002 \text{ mm day}^{-1}$ . The maximum cooling ( $\sim 1 \text{ K}$ ) due  
637 to fire aerosols occurs around  $60^\circ\text{N}$  in summer, and a suppression of precipitation  
638 ( $\sim 0.1 \text{ mm day}^{-1}$ ) is also found there. The strong cooling is a result of the strong  
639 indirect effects ( $-15 \text{ W m}^{-2}$ ) in the land areas of the Arctic regions ( $60^\circ\text{N}$  to  $90^\circ\text{N}$ ). A  
640 significant reduction of precipitation in southern Africa is also noticed. We note that  
641 these results are based on the simulations with fixed SSTs and may not represent the  
642 full climate responses.

643 In our study, the global radiative effect of fire aerosols is estimated from  
644 simulations performed with the 4-mode version Modal aerosol module (MAM4) [*Liu*  
645 *et al.*, 2016], daily fire emissions with prescribed vertical emission profiles, and  
646 higher model resolution ( $0.9^\circ$  by  $1.25^\circ$ ) compared to earlier modeling studies of fire  
647 aerosols [*Tosca et al.*, 2013; *Ward et al.*, 2012]. In their studies, the GFED fire  
648 aerosol emissions were increased by a factor of 1-3 depending on regions to match the

649 observed AOD. In our study, we do not apply the scaling factor to the fire aerosol  
650 emissions. Our global annual mean RE<sub>ari</sub> of fire aerosols ( $0.16 \pm 0.01 \text{ W m}^{-2}$ ) is,  
651 however, close to  $0.18 \text{ W m}^{-2}$  in *Tosca et al.* [2013] and  $0.13 \text{ W m}^{-2}$  in *Ward et al.*  
652 [2012]. The similar fire aerosol RE<sub>ari</sub> from our study but with smaller fire emissions  
653 than these previous studies can result from (1) the use of MAM4 in our study which  
654 more realistically represents the external/internal mixing of BC with other soluble  
655 aerosol species; (2) the more accurate estimation of RE<sub>ari</sub> of fire aerosols in the  
656 presence of low-level clouds with the method of *Ghan* [2013]; and (3) the inclusion of  
657 vertical emissions of fire aerosols, which allows more efficient transport of fire  
658 aerosols from sources. The RE<sub>aci</sub> due to fire aerosols in our study ( $-0.70 \pm 0.05 \text{ W m}^{-2}$ )  
659 is smaller than  $-1.64 \text{ W m}^{-2}$  in *Ward et al.* [2012] due to the lower fire POM emissions  
660 used in this study compared to *Ward et al.* [2012].

661 We note that there are limitations and uncertainties with our study. The model  
662 still underestimates observed AODs (mostly within a factor of 2) at the sites  
663 predominantly influenced by biomass burning aerosols during the fire season, which  
664 implies that the fire aerosol radiative forcing can be stronger than estimated in this  
665 study. The RE estimates of fire POM and fire BC with the *Ghan* [2013] approach may  
666 not be accurate due to the internal mixing of co-emitted fire components (POM and  
667 BC). In our simulations, sea ice is prescribed, and thus the fire BC effect on sea ice  
668 albedo is not considered. The brown carbon component of POM [*Feng et al.*, 2013] is  
669 not treated in the current CESM model, which may result in an underestimation of  
670 atmospheric absorption of fire aerosols.

671

672 **Acknowledgments**

673 This work is supported by the Office of Science of the US Department of Energy  
674 (DOE) as the NSF-DOE-USDA Joint Earth System Modeling (EaSM) Program, the  
675 National Key Basic Research Program (973 Program) of China under Grant No.  
676 2010CB428504, and the National Natural Science Foundation of China (NSFC) under  
677 Grant No.41505062. The Pacific Northwest National Laboratory is operated for the  
678 DOE by the Battelle Memorial Institute under contract DE-AC05-76RL01830. The  
679 authors would like to acknowledge the use of computational resources  
680 (ark:/85065/d7wd3xhc) at the NCAR-Wyoming Supercomputing Center provided by  
681 the National Science Foundation and the State of Wyoming, and supported by  
682 NCAR's Computational and Information Systems Laboratory. The fire emission data  
683 were obtained from the Global Fire Emissions Database (GFED,  
684 <http://www.globalfiredata.org>). The AERONET data were obtained from  
685 <http://aeronet.gsfc.nasa.gov>. We thank Xiangjun Shi for the help with processing the  
686 AERONET data.

687

688 **References**

689

690 Abel, S. J., Highwood, E. J., Haywood, J. M., and Stringer, M. A.: The direct  
691 radiative effect of biomass burning aerosols over southern Africa, *Atmos. Chem.*  
692 *Phys.*, 5, 1999-2018, 10.5194/acp-5-1999-2005, 2005.  
693 Ackerman, A. S., Toon, O. B., Stevens, D. E., Heymsfield, A. J., Ramanathan, V., and  
694 Welton, E. J.: Reduction of Tropical Cloudiness by Soot, *Science*, 288, 1042-1047,  
695 10.1126/science.288.5468.1042, 2000.  
696 Andreae, M. O., and Rosenfeld, D.: Aerosol–cloud–precipitation interactions. Part 1.

697 The nature and sources of cloud-active aerosols, *Earth-Science Reviews*, 89,  
698 13-41, <http://dx.doi.org/10.1016/j.earscirev.2008.03.001>, 2008.

699 Andreae, M. O., Rosenfeld, D., Artaxo, P., Costa, A. A., Frank, G. P., Longo, K. M.,  
700 and Silva-Dias, M. A. F.: Smoking Rain Clouds over the Amazon, *Science*, 303,  
701 1337-1342, [10.1126/science.1092779](https://doi.org/10.1126/science.1092779), 2004.

702 Bistinas, I., Harrison, S. P., Prentice, I. C., and Pereira, J. M. C.: Causal relationships  
703 versus emergent patterns in the global controls of fire frequency, *Biogeosciences*,  
704 11, 5087-5101, [10.5194/bg-11-5087-2014](https://doi.org/10.5194/bg-11-5087-2014), 2014.

705 Bond, T. C., Doherty, S. J., Fahey, D. W., Forster, P. M., Berntsen, T., DeAngelo, B.  
706 J., Flanner, M. G., Ghan, S., Karcher, B., Koch, D., Kinne, S., Kondo, Y., Quinn,  
707 P. K., Sarofim, M. C., Schultz, M. G., Schulz, M., Venkataraman, C., Zhang, H.,  
708 Zhang, S., Bellouin, N., Guttikunda, S. K., Hopke, P. K., Jacobson, M. Z., Kaiser,  
709 J. W., Klimont, Z., Lohmann, U., Schwarz, J. P., Shindell, D., Storelvmo, T.,  
710 Warren, S. G., and Zender, C. S.: Bounding the role of black carbon in the climate  
711 system: A scientific assessment, *J Geophys Res-Atmos*, 118, 5380-5552, [Doi  
712 10.1002/Jgrd.50171](https://doi.org/10.1002/Jgrd.50171), 2013.

713 Boucher, O., and Tanré, D.: Estimation of the aerosol perturbation to the Earth's  
714 Radiative Budget over oceans using POLDER satellite aerosol retrievals,  
715 *Geophysical Research Letters*, 27, 1103-1106, [10.1029/1999GL010963](https://doi.org/10.1029/1999GL010963), 2000.

716 Bowman, D. M. J. S., Balch, J. K., Artaxo, P., Bond, W. J., Carlson, J. M., Cochrane,  
717 M. A., D'Antonio, C. M., DeFries, R. S., Doyle, J. C., Harrison, S. P., Johnston, F.  
718 H., Keeley, J. E., Krawchuk, M. A., Kull, C. A., Marston, J. B., Moritz, M. A.,  
719 Prentice, I. C., Roos, C. I., Scott, A. C., Swetnam, T. W., van der Werf, G. R., and  
720 Pyne, S. J.: Fire in the Earth System, *Science*, 324, 481-484,  
721 [10.1126/science.1163886](https://doi.org/10.1126/science.1163886), 2009.

722 Carslaw, K. S., Boucher, O., Spracklen, D. V., Mann, G. W., Rae, J. G. L., Woodward,  
723 S., and Kulmala, M.: A review of natural aerosol interactions and feedbacks  
724 within the Earth system, *Atmos. Chem. Phys.*, 10, 1701-1737,  
725 [10.5194/acp-10-1701-2010](https://doi.org/10.5194/acp-10-1701-2010), 2010.

726 Chakrabarty, R. K., Beres, N. D., Moosmüller, H., China, S., Mazzoleni, C., Dubey,

727 M. K., Liu, L., and Mishchenko, M. I.: Soot superaggregates from flaming  
728 wildfires and their direct radiative forcing, *Scientific Reports*, 4, 5508,  
729 10.1038/srep05508.

730 Ciais, P., Sabine, C., Bala, G., Bopp, L., Brovkin, V., Canadell, J., Chhabra, A.,  
731 DeFries, R., Galloway, J., Heimann, M., Jones, C., Le Quéré, C., Myneni, R. B.,  
732 Piao, S., and Thornton, P.: Carbon and Other Biogeochemical Cycles, in: *Climate*  
733 *Change 2013: The Physical Science Basis. Contribution of Working Group I to*  
734 *the Fifth Assessment Report of the Intergovernmental Panel on Climate Change*,  
735 edited by: Stocker, T. F., Qin, D., Plattner, G.-K., Tignor, M., Allen, S. K.,  
736 Boschung, J., Nauels, A., Xia, Y., Bex, V., and Midgley, P. M., Cambridge  
737 University Press, Cambridge, United Kingdom and New York, NY, USA, 465–  
738 570, 2013.

739 Cohen, J. B., and Wang, C.: Estimating global black carbon emissions using a  
740 top-down Kalman Filter approach, *Journal of Geophysical Research: Atmospheres*,  
741 119, 2013JD019912, 10.1002/2013JD019912, 2014.

742 Dentener, F., Kinne, S., Bond, T., Boucher, O., Cofala, J., Generoso, S., Ginoux, P.,  
743 Gong, S., Hoelzemann, J. J., Ito, A., Marelli, L., Penner, J. E., Putaud, J. P.,  
744 Textor, C., Schulz, M., van der Werf, G. R., and Wilson, J.: Emissions of primary  
745 aerosol and precursor gases in the years 2000 and 1750 prescribed data-sets for  
746 AeroCom, *Atmos. Chem. Phys.*, 6, 4321-4344, 10.5194/acp-6-4321-2006, 2006.

747 Doherty, S. J., Warren, S. G., Grenfell, T. C., Clarke, A. D., and Brandt, R. E.:  
748 Light-absorbing impurities in Arctic snow, *Atmos. Chem. Phys.*, 10, 11647-11680,  
749 10.5194/acp-10-11647-2010, 2010.

750 Feng, Y., V. Ramanathan, and V. R. Kotamarthi: Brown carbon: a significant  
751 atmospheric absorber of solar radiation?, *Atmos. Chem. Phys.*, 13(17), 8607–8621,  
752 doi:10.5194/acp-13-8607-2013, 2013.

753 Flanner, M. G., and Zender, C. S.: Snowpack radiative heating: Influence on Tibetan  
754 Plateau climate, *Geophysical Research Letters*, 32, L06501, Artn L06501, Doi  
755 10.1029/2004gl022076, 2005.

756 Flanner, M. G., Zender, C. S., Randerson, J. T., and Rasch, P. J.: Present-day climate

757 forcing and response from black carbon in snow, *Journal of Geophysical Research:*  
758 *Atmospheres*, 112, D11202, 10.1029/2006JD008003, 2007.

759 Flanner, M. G., Zender, C. S., Hess, P. G., Mahowald, N. M., Painter, T. H.,  
760 Ramanathan, V., and Rasch, P. J.: Springtime warming and reduced snow cover  
761 from carbonaceous particles, *Atmos. Chem. Phys.*, 9, 2481-2497,  
762 10.5194/acp-9-2481-2009, 2009.

763 Forster, P., Ramaswamy, V., Artaxo, P., Berntsen, T., Betts, R., Fahey, D. W.,  
764 Haywood, J., Lean, J., Lowe, D. C., and Myhre, G.: Changes in atmospheric  
765 constituents and in radiative forcing. Chapter 2, in: *Climate Change 2007. The*  
766 *Physical Science Basis*, 2007.

767 Ghan, S. J.: Technical Note: Estimating aerosol effects on cloud radiative forcing,  
768 *Atmos. Chem. Phys.*, 13, 9971-9974, 10.5194/acp-13-9971-2013, 2013.

769 Ghan, S. J., Liu, X., Easter, R. C., Zaveri, R., Rasch, P. J., Yoon, J.-H., and Eaton, B.:  
770 Toward a Minimal Representation of Aerosols in Climate Models: Comparative  
771 Decomposition of Aerosol Direct, Semidirect, and Indirect Radiative Forcing,  
772 *Journal of Climate*, 25, 6461-6476, doi:10.1175/JCLI-D-11-00650.1, 2012.

773 Giglio, L., Randerson, J. T., and van der Werf, G. R.: Analysis of daily, monthly, and  
774 annual burned area using the fourth-generation global fire emissions database  
775 (GFED4), *Journal of Geophysical Research: Biogeosciences*, 118, 317-328,  
776 10.1002/jgrg.20042, 2013.

777 Hansen, J., Sato, M., Ruedy, R., Nazarenko, L., Lacis, A., Schmidt, G. A., Russell, G.,  
778 Aleinov, I., Bauer, M., Bauer, S., Bell, N., Cairns, B., Canuto, V., Chandler, M.,  
779 Cheng, Y., Del Genio, A., Faluvegi, G., Fleming, E., Friend, A., Hall, T., Jackman,  
780 C., Kelley, M., Kiang, N., Koch, D., Lean, J., Lerner, J., Lo, K., Menon, S., Miller,  
781 R., Minnis, P., Novakov, T., Oinas, V., Perlwitz, J., Perlwitz, J., Rind, D.,  
782 Romanou, A., Shindell, D., Stone, P., Sun, S., Tausnev, N., Thresher, D., Wielicki,  
783 B., Wong, T., Yao, M., and Zhang, S.: Efficacy of climate forcings, *Journal of*  
784 *Geophysical Research: Atmospheres*, 110, D18104, 10.1029/2005JD005776,  
785 2005.

786 Heald, C. L., Ridley, D. A., Kroll, J. H., Barrett, S. R. H., Cady-Pereira, K. E.,

787 Alvarado, M. J., and Holmes, C. D.: Contrasting the direct radiative effect and  
788 direct radiative forcing of aerosols, *Atmos. Chem. Phys.*, 14, 5513-5527,  
789 10.5194/acp-14-5513-2014, 2014.

790 Houghton, J. T.: *Climate change 1995: The science of climate change: contribution of*  
791 *working group I to the second assessment report of the Intergovernmental Panel*  
792 *on Climate Change*, Cambridge University Press, 1996.

793 IPCC (2013), *Climate Change 2013: The Physical Science Basis. Contribution of*  
794 *Working Group I to the Fifth Assessment Report of the Intergovernmental Panel*  
795 *on Climate Change*, 1535 pp., Cambridge University Press, Cambridge, United  
796 Kingdom and New York, NY, USA, doi:10.1017/CBO9781107415324.

797 Jacobson, M. Z.: Climate response of fossil fuel and biofuel soot, accounting for  
798 soot's feedback to snow and sea ice albedo and emissivity, *Journal of Geophysical*  
799 *Research: Atmospheres*, 109, D21201, 10.1029/2004JD004945, 2004.

800 Jiang, Y., Liu, X., Yang, X.-Q., and Wang, M.: A numerical study of the effect of  
801 different aerosol types on East Asian summer clouds and precipitation,  
802 *Atmospheric Environment*, 70, 51-63,  
803 <http://dx.doi.org/10.1016/j.atmosenv.2012.12.039>, 2013.

804 Jiang, Y., Yang, X.-Q., and Liu, X.: Seasonality in anthropogenic aerosol effects on  
805 East Asian climate simulated with CAM5, *Journal of Geophysical Research:*  
806 *Atmospheres*, 120, 2015JD023451, 10.1002/2015JD023451, 2015.

807 Jones, A., Haywood, J. M., and Boucher, O.: Aerosol forcing, climate response and  
808 climate sensitivity in the Hadley Centre climate model, *Journal of Geophysical*  
809 *Research: Atmospheres*, 112, D20211, 10.1029/2007JD008688, 2007.

810 Kaiser, J. W., Heil, A., Andreae, M. O., Benedetti, A., Chubarova, N., Jones, L.,  
811 Morcrette, J. J., Razinger, M., Schultz, M. G., Suttie, M., and van der Werf, G. R.:  
812 Biomass burning emissions estimated with a global fire assimilation system based  
813 on observed fire radiative power, *Biogeosciences*, 9, 527-554,  
814 10.5194/bg-9-527-2012, 2012.

815 Keywood, M., Kanakidou, M., Stohl, A., Dentener, F., Grassi, G., Meyer, C. P.,  
816 Torseth, K., Edwards, D., Thompson, A. M., Lohmann, U., and Burrows, J.: Fire

817 in the Air: Biomass Burning Impacts in a Changing Climate, *Critical Reviews in*  
818 *Environmental Science and Technology*, 43, 40-83,  
819 10.1080/10643389.2011.604248, 2011.

820 Koch, D., Menon, S., Del Genio, A., Ruedy, R., Alienov, I., and Schmidt, G. A.:  
821 Distinguishing Aerosol Impacts on Climate over the Past Century, *Journal of*  
822 *Climate*, 22, 2659-2677, 10.1175/2008JCLI2573.1, 2009.

823 Koch, D., Balkanski, Y., Bauer, S. E., Easter, R. C., Ferrachat, S., Ghan, S. J., Hoose,  
824 C., Iversen, T., Kirkevåg, A., Kristjansson, J. E., Liu, X., Lohmann, U., Menon, S.,  
825 Quaas, J., Schulz, M., Seland, Ø., Takemura, T., and Yan, N.: Soot microphysical  
826 effects on liquid clouds, a multi-model investigation, *Atmos. Chem. Phys.*, 11,  
827 1051-1064, 10.5194/acp-11-1051-2011, 2011.

828 Koch, D., and Del Genio, A. D.: Black carbon semi-direct effects on cloud cover:  
829 review and synthesis, *Atmos. Chem. Phys.*, 10, 7685-7696,  
830 10.5194/acp-10-7685-2010, 2010.

831 Koren, I., Kaufman, Y. J., Rosenfeld, D., Remer, L. A., and Rudich, Y.: Aerosol  
832 invigoration and restructuring of Atlantic convective clouds, *Geophysical*  
833 *Research Letters*, 32, L14828, 10.1029/2005GL023187, 2005.

834 Lamarque, J. F., Bond, T. C., Eyring, V., Granier, C., Heil, A., Klimont, Z., Lee, D.,  
835 Liousse, C., Mieville, A., Owen, B., Schultz, M. G., Shindell, D., Smith, S. J.,  
836 Stehfest, E., Van Aardenne, J., Cooper, O. R., Kainuma, M., Mahowald, N.,  
837 McConnell, J. R., Naik, V., Riahi, K., and van Vuuren, D. P.: Historical (1850–  
838 2000) gridded anthropogenic and biomass burning emissions of reactive gases and  
839 aerosols: methodology and application, *Atmos. Chem. Phys.*, 10, 7017-7039,  
840 10.5194/acp-10-7017-2010, 2010.

841 Liu, X., J. E. Penner, B. Das, D. Bergmann, J. M. Rodriguez, S. Strahan, M. Wang  
842 and Y. Feng: Uncertainties in global aerosol simulations: Assessment using three  
843 meteorological datasets, *Journal of Geophysical Research*, 112, D11212,  
844 doi:10.1029/2006JD008216, 2007.

845 Liu, X., Easter, R. C., Ghan, S. J., Zaveri, R., Rasch, P., Shi, X., Lamarque, J. F.,  
846 Gettelman, A., Morrison, H., Vitt, F., Conley, A., Park, S., Neale, R., Hannay, C.,



847 Ekman, A. M. L., Hess, P., Mahowald, N., Collins, W., Iacono, M. J., Bretherton,  
848 C. S., Flanner, M. G., and Mitchell, D.: Toward a minimal representation of  
849 aerosols in climate models: description and evaluation in the Community  
850 Atmosphere Model CAM5, *Geosci. Model Dev.*, 5, 709-739,  
851 10.5194/gmd-5-709-2012, 2012.

852 Liu, X., Ma, P. L., Wang, H., Tilmes, S., Singh, B., Easter, R. C., Ghan, S. J., and  
853 Rasch, P. J.: Description and evaluation of a new four-mode version of the Modal  
854 Aerosol Module (MAM4) within version 5.3 of the Community Atmosphere  
855 Model, *Geosci. Model Dev.*, 9, 505-522, 10.5194/gmd-9-505-2016, 2016.

856 Liu, Y.: Atmospheric response and feedback to radiative forcing from biomass  
857 burning in tropical South America, *Agricultural and Forest Meteorology*, 133,  
858 40-53, <http://dx.doi.org/10.1016/j.agrformet.2005.03.011>, 2005.

859 Liu, Y., Goodrick, S., and Heilman, W.: Wildland fire emissions, carbon, and climate:  
860 Wildfire–climate interactions, *Forest Ecology and Management*, 317, 80-96,  
861 <http://dx.doi.org/10.1016/j.foreco.2013.02.020>, 2014.

862 Lu, Z., and Sokolik, I. N.: The effect of smoke emission amount on changes in cloud  
863 properties and precipitation: A case study of Canadian boreal wildfires of 2007,  
864 *Journal of Geophysical Research: Atmospheres*, 118, 2013JD019860,  
865 10.1002/2013JD019860, 2013.

866 Ma, P.-L., P. J. Rasch, H. Wang, K. Zhang, R. C. Easter, S. Tilmes, J. D. Fast, X. Liu,  
867 J.-H. Yoon, and J.-F. Lamarque: The role of circulation features on black carbon  
868 transport into the Arctic in the Community Atmosphere Model version 5 (CAM5),  
869 *J. Geophys. Res. Atmos.*, 118, 4657–4669, 2013.

870 Ma, P. L., Rasch, P. J., Fast, J. D., Easter, R. C., Gustafson Jr, W. I., Liu, X., Ghan, S.  
871 J., and Singh, B.: Assessing the CAM5 physics suite in the WRF-Chem model:  
872 implementation, resolution sensitivity, and a first evaluation for a regional case  
873 study, *Geosci. Model Dev.*, 7, 755-778, 10.5194/gmd-7-755-2014, 2014.

874 Ma, P.-L., P. J. Rasch, M. Wang, H. Wang, S. J. Ghan, R. C. Easter, W. I. Gustafson  
875 Jr., X. Liu, Y. Zhang, and H.-Y. Ma: How does increasing horizontal resolution in  
876 a global climate model improve the simulation of aerosol-cloud interactions?,

877 Geophys. Res. Lett., 42, 5058–5065, doi:10.1002/2015GL064183, 2015.

878 Marlon, J. R., Bartlein, P. J., Walsh, M. K., Harrison, S. P., Brown, K. J., Edwards, M.  
879 E., Higuera, P. E., Power, M. J., Anderson, R. S., Briles, C., Brunelle, A.,  
880 Carcaillet, C., Daniels, M., Hu, F. S., Lavoie, M., Long, C., Minckley, T., Richard,  
881 P. J. H., Scott, A. C., Shafer, D. S., Tinner, W., Umbanhowar, C. E., and Whitlock,  
882 C.: Wildfire responses to abrupt climate change in North America, Proceedings of  
883 the National Academy of Sciences, 106, 2519-2524, 10.1073/pnas.0808212106,  
884 2009.

885 McCarthy, J. J.: Climate change 2001: impacts, adaptation, and vulnerability:  
886 contribution of Working Group II to the third assessment report of the  
887 Intergovernmental Panel on Climate Change, Cambridge University Press, 2001.

888 Min M., and Zhang Z.: On the influence of cloud fraction diurnal cycle and sub-grid  
889 cloud optical thickness variability on all-sky direct aerosol radiative forcing, J.  
890 Quant. Spectros. Radiat. Transfer, doi:10.1016/j.jqsrt.2014.03.014, 2014.

891 Morrison, H., and Gettelman, A.: A New Two-Moment Bulk Stratiform Cloud  
892 Microphysics Scheme in the Community Atmosphere Model, Version 3 (CAM3).  
893 Part I: Description and Numerical Tests, Journal of Climate, 21, 3642-3659,  
894 doi:10.1175/2008JCLI2105.1, 2008.

895 Myhre, G., Samset, B. H., Schulz, M., Balkanski, Y., Bauer, S., Berntsen, T. K., Bian,  
896 H., Bellouin, N., Chin, M., Diehl, T., Easter, R. C., Feichter, J., Ghan, S. J.,  
897 Hauglustaine, D., Iversen, T., Kinne, S., Kirkevåg, A., Lamarque, J. F., Lin, G.,  
898 Liu, X., Lund, M. T., Luo, G., Ma, X., van Noije, T., Penner, J. E., Rasch, P. J.,  
899 Ruiz, A., Seland, Ø., Skeie, R. B., Stier, P., Takemura, T., Tsigaridis, K., Wang,  
900 P., Wang, Z., Xu, L., Yu, H., Yu, F., Yoon, J. H., Zhang, K., Zhang, H., and Zhou,  
901 C.: Radiative forcing of the direct aerosol effect from AeroCom Phase II  
902 simulations, Atmos. Chem. Phys., 13, 1853-1877, 10.5194/acp-13-1853-2013,  
903 2013.

904 Myhre, G., Shindell, D., Bréon, F.-M., Collins, W., Fuglestvedt, J., Huang, J., Koch,  
905 D., Lamarque, J.-F., Lee, D., Mendoza, B., Nakajima, T., Robock, A., Stephens,  
906 G., Takemura, T., and Zhang, H.: Anthropogenic and Natural Radiative Forcing,

907 in: *Climate Change 2013: The Physical Science Basis. Contribution of Working*  
908 *Group I to the Fifth Assessment Report of the Intergovernmental Panel on Climate*  
909 *Change*, edited by: Stocker, T. F., Qin, D., Plattner, G.-K., Tignor, M., Allen, S.  
910 K., Boschung, J., Nauels, A., Xia, Y., Bex, V., and Midgley, P. M., Cambridge  
911 University Press, Cambridge, United Kingdom and New York, NY, USA, 659–  
912 740, 2013.

913 Myhre, G., and Samset, B. H.: Standard climate models radiation codes underestimate  
914 black carbon radiative forcing, *Atmos. Chem. Phys.*, 15, 2883-2888,  
915 10.5194/acp-15-2883-2015, 2015.

916 Neale, R., Chen, C., Gettelman, A., Lauritzen, P., Park, S., Williamson, D., Garcia, R.,  
917 Kinnison, D., Lamarque, J., and Marsh, D.: Description of the NCAR Community  
918 Atmosphere Model (CAM 5.0), 2010.

919 Oleson, K. W., Lawrence, D. M., Gordon, B., Flanner, M. G., Kluzek, E., Peter, J.,  
920 Levis, S., Swenson, S. C., Thornton, E., and Feddema, J.: Technical description of  
921 version 4.0 of the Community Land Model (CLM), 2010.

922 Peng, Y., Lohmann, U., Leaitch, R., Banic, C., and Couture, M.: The cloud  
923 albedo-cloud droplet effective radius relationship for clean and polluted clouds  
924 from RACE and FIRE.ACE, *Journal of Geophysical Research: Atmospheres*, 107,  
925 AAC 1-1-AAC 1-6, 10.1029/2000JD000281, 2002.

926 Qian, Y., Flanner, M. G., Leung, L. R., and Wang, W.: Sensitivity studies on the  
927 impacts of Tibetan Plateau snowpack pollution on the Asian hydrological cycle  
928 and monsoon climate, *Atmos. Chem. Phys.*, 11, 1929-1948,  
929 10.5194/acp-11-1929-2011, 2011.

930 Qian, Y., Gong, D., Fan, J., Leung, L. R., Bennartz, R., Chen, D., and Wang, W.:  
931 Heavy pollution suppresses light rain in China: Observations and modeling,  
932 *Journal of Geophysical Research: Atmospheres*, 114, D00K02,  
933 10.1029/2008JD011575, 2009.

934 Qian, Y., Wang, H., Zhang, R., Flanner, M. G., and Rasch, P. J.: A sensitivity study  
935 on modeling black carbon in snow and its radiative forcing over the Arctic and  
936 Northern China, *Environmental Research Letters*, 9, 064001,

937 10.1088/1748-9326/9/6/064001, 2014.

938 Qian, Y., Yasunari, T. J., Doherty, S. J., Flanner, M. G., Lau, W. K. M., Ming, J.,  
939 Wang, H., Wang, M., Warren, S. G., and Zhang, R.: Light-absorbing particles in  
940 snow and ice: Measurement and modeling of climatic and hydrological impact,  
941 *Advances in Atmospheric Sciences*, 32, 64-91, 10.1007/s00376-014-0010-0,  
942 2015.

943 Quinn, P. K., Bates, T. S., Baum, E., Doubleday, N., Fiore, A. M., Flanner, M.,  
944 Fridlind, A., Garrett, T. J., Koch, D., Menon, S., Shindell, D., Stohl, A., and  
945 Warren, S. G.: Short-lived pollutants in the Arctic: their climate impact and  
946 possible mitigation strategies, *Atmos. Chem. Phys.*, 8, 1723-1735,  
947 10.5194/acp-8-1723-2008, 2008.

948 Randerson, J. T., Liu, H., Flanner, M. G., Chambers, S. D., Jin, Y., Hess, P. G.,  
949 Pfister, G., Mack, M. C., Treseder, K. K., Welp, L. R., Chapin, F. S., Harden, J.  
950 W., Goulden, M. L., Lyons, E., Neff, J. C., Schuur, E. A. G., and Zender, C. S.:  
951 The Impact of Boreal Forest Fire on Climate Warming, *Science*, 314, 1130-1132,  
952 2006.

953 Rypdal, K., Rive, N., Berntsen, T. K., Klimont, Z., Mideksa, T. K., Myhre, G., and  
954 Skeie, R. B.: Costs and global impacts of black carbon abatement strategies,  
955 *Tellus B*, 61, 625-641, 10.1111/j.1600-0889.2009.00430.x, 2009.

956 Sena, E. T., and Artaxo, P.: A novel methodology for large-scale daily assessment of  
957 the direct radiative forcing of smoke aerosols, *Atmospheric Chemistry and  
958 Physics*, 15, 5471-5483, 10.5194/acp-15-5471-2015, 2015.

959 Skeie, R. B., Berntsen, T., Myhre, G., Pedersen, C. A., Ström, J., Gerland, S., and  
960 Ogren, J. A.: Black carbon in the atmosphere and snow, from pre-industrial times  
961 until present, *Atmos. Chem. Phys.*, 11, 6809-6836, 10.5194/acp-11-6809-2011,  
962 2011.

963 Sommers, W. T., Loehman, R. A., and Hardy, C. C.: Wildland fire emissions, carbon,  
964 and climate: Science overview and knowledge needs, *Forest Ecology and  
965 Management*, 317, 1-8, <http://dx.doi.org/10.1016/j.foreco.2013.12.014>, 2014.

966 Stohl, A., Klimont, Z., Eckhardt, S., Kupiainen, K., Shevchenko, V. P., Kopeikin, V.

967 M., and Novigatsky, A. N.: Black carbon in the Arctic: the underestimated role of  
968 gas flaring and residential combustion emissions, *Atmos. Chem. Phys.*, 13,  
969 8833-8855, 10.5194/acp-13-8833-2013, 2013.

970 Tosca, M. G., Diner, D. J., Garay, M. J., and Kalashnikova, O. V.: Observational  
971 evidence of fire-driven reduction of cloud fraction in tropical Africa, *Journal of*  
972 *Geophysical Research: Atmospheres*, 2014JD021759, 10.1002/2014JD021759,  
973 2014.

974 Tosca, M. G., Randerson, J. T., and Zender, C. S.: Global impact of smoke aerosols  
975 from landscape fires on climate and the Hadley circulation, *Atmos. Chem. Phys.*,  
976 13, 5227-5241, 10.5194/acp-13-5227-2013, 2013.

977 van der Werf, G. R., Dempewolf, J., Trigg, S. N., Randerson, J. T., Kasibhatla, P. S.,  
978 Giglio, L., Murdiyarso, D., Peters, W., Morton, D. C., Collatz, G. J., Dolman, A.  
979 J., and DeFries, R. S.: Climate regulation of fire emissions and deforestation in  
980 equatorial Asia, *Proceedings of the National Academy of Sciences*, 105,  
981 20350-20355, 10.1073/pnas.0803375105, 2008.

982 van der Werf, G. R., Randerson, J. T., Giglio, L., Collatz, G. J., Mu, M., Kasibhatla, P.  
983 S., Morton, D. C., DeFries, R. S., Jin, Y., and van Leeuwen, T. T.: Global fire  
984 emissions and the contribution of deforestation, savanna, forest, agricultural, and  
985 peat fires (1997–2009), *Atmos. Chem. Phys.*, 10, 11707-11735,  
986 10.5194/acp-10-11707-2010, 2010.

987 Voulgarakis, A., and Field, R. D.: Fire influences on atmospheric composition, air  
988 quality and climate, *Current Pollution Reports*, 1, 70-81,  
989 10.1007/s40726-015-0007-z, 2015.

990 Wang, H., Easter, R. C., Rasch, P. J., Wang, M., Liu, X., Ghan, S. J., Qian, Y., Yoon,  
991 J. H., Ma, P. L., and Vinoj, V.: Sensitivity of remote aerosol distributions to  
992 representation of cloud–aerosol interactions in a global climate model, *Geosci.*  
993 *Model Dev.*, 6, 765-782, 10.5194/gmd-6-765-2013, 2013a.

994 Wang, X., Doherty, S. J., and Huang, J.: Black carbon and other light-absorbing  
995 impurities in snow across Northern China, *Journal of Geophysical Research:*  
996 *Atmospheres*, 118, 1471-1492, 10.1029/2012JD018291, 2013b.

997 Ward, D. S., Kloster, S., Mahowald, N. M., Rogers, B. M., Randerson, J. T., and Hess,  
998 P. G.: The changing radiative forcing of fires: global model estimates for past,  
999 present and future, *Atmos. Chem. Phys.*, 12, 10857-10886,  
1000 10.5194/acp-12-10857-2012, 2012.

1001 Westerling, A. L., Hidalgo, H. G., Cayan, D. R., and Swetnam, T. W.: Warming and  
1002 earlier spring increase western U.S. forest wildfire activity, *Science*, 313, 940-943,  
1003 10.1126/science.1128834, 2006.

1004 Wiedinmyer, C., Akagi, S. K., Yokelson, R. J., Emmons, L. K., Al-Saadi, J. A.,  
1005 Orlando, J. J., and Soja, A. J.: The Fire INventory from NCAR (FINN): a high  
1006 resolution global model to estimate the emissions from open burning, *Geosci.*  
1007 *Model Dev.*, 4, 625-641, 10.5194/gmd-4-625-2011, 2011.

1008 Zhang, Y., Fu, R., Yu, H., Qian, Y., Dickinson, R., Silva Dias, M. A. F., da Silva Dias,  
1009 P. L., and Fernandes, K.: Impact of biomass burning aerosol on the monsoon  
1010 circulation transition over Amazonia, *Geophysical Research Letters*, 36, L10814,  
1011 10.1029/2009GL037180, 2009.

1012 Zhang, Z., Meyer, K., Platnick, S., Oreopoulos, L., Lee, D., and Yu, H.: A novel  
1013 method for estimating shortwave direct radiative effect of above-cloud aerosols  
1014 using CALIOP and MODIS data, *Atmos. Meas. Tech.*, 7, 1777-1789,  
1015 10.5194/amt-7-1777-2014, 2014.

1016 Zhang, Z., Meyer, K., Yu, H., Platnick, S., Colarco, P., Liu, Z., and Oreopoulos, L.:  
1017 Shortwave direct radiative effects of above-cloud aerosols over global oceans  
1018 derived from 8 years of CALIOP and MODIS observations, *Atmos. Chem. Phys.*,  
1019 16, 2877-2900, 10.5194/acp-16-2877-2016, 2016.

1020

1021 **Figure Captions**

1022

1023 Figure 1. Seasonal variation of GFED monthly fire (a) organic carbon (OC) and (b)  
1024 black carbon (BC) emissions ( $\text{Tg C month}^{-1}$ ) averaged for the period of year 2003 to  
1025 2011 in the global, tropical ( $25^{\circ}\text{S}$  to  $25^{\circ}\text{N}$ ) and Arctic ( $60^{\circ}\text{N}$  to  $90^{\circ}\text{N}$ ) regions.

1026

1027 Figure 2. Comparison of modeled seasonal variations of aerosol optical depth (AOD)  
1028 for the period of 2003-2011 with observations for the same period from the  
1029 AERONET sites. The upper, middle, and bottom panels represent the sites in southern  
1030 Africa, South America, and the Arctic, respectively.

1031

1032 Figure 3. Same as Figure 2, but for the comparison of single scattering albedo (SSA)  
1033 at 550 nm.

1034

1035 Figure 4. Annual mean radiative effect due to aerosol-radiation interactions (REari)  
1036 ( $\text{W m}^{-2}$ ) averaged over the period of 2003-2011 due to (a) all fire aerosols, (c) fire BC,  
1037 and (e) fire POM estimated with the method of BBFFBF (left panels), and with the  
1038 method of Ghan (2013) ((b), (d), and (f) in the right panels). The plus signs in Figure  
1039 4(b), (d) and (f) denote the regions where the radiative effect estimated with Ghan  
1040 [2013] is statistically significant at the 0.05 level.

1041

1042 Figure 5. (a) September-October-November (SON) mean fire aerosol radiative effect  
1043 due to aerosol-radiation interactions (REari) ( $\text{W m}^{-2}$ ) for the period of 2003-2011 over  
1044 the Southeast Atlantic Ocean due to all fire aerosols. (b) and (c) are the same as (a),  
1045 but for the above-cloud aerosol REari for the period of 2007-2011 estimated using  
1046 Aqua/MODIS and Terra/MODIS products [Zhang *et al.*, 2014], respectively.

1047

1048 Figure 6. Annual mean radiative effect due to aerosol-cloud interactions (REaci) ( $\text{W}$   
1049  $\text{m}^{-2}$ ) averaged over the period of 2003-2011 due to (a) all fire aerosols, (b) fire BC,  
1050 and (c) fire POM. The plus signs denote the regions where the radiative effect is  
1051 statistically significant at the 0.1 level.

1052

1053 Figure 7. Seasonal variation of radiative effect of all fire aerosols due to aerosol-cloud  
1054 interactions (REaci) ( $\text{W m}^{-2}$ ) for the period of 2003-2011 for (a)  
1055 December-January-February (DJF), (b) March-April-May (MAM), (c)  
1056 June-July-August (JJA), and (d) September-October-November (SON). The plus signs  
1057 denote the regions where the radiative effect is statistically significant at the 0.05  
1058 level.

1059

1060 Figure 8. Month-latitude cross sections of zonal mean and monthly (a)  
1061 vertically-integrated concentrations ( $\text{mg m}^{-2}$ ) of fire BC and (b) fire POM, (c) cloud  
1062 liquid water path (LWP, in  $\text{g m}^{-2}$ ), (d) low-level cloud cover (CLDLow, in %), (e)  
1063 radiative effect due to aerosol-radiation interactions (REari, in  $\text{W m}^{-2}$ ), and (f)  
1064 radiative effect due to aerosol-cloud interactions (REaci, in  $\text{W m}^{-2}$ ) of all fire aerosols.

1065

1066 Figure 9. Evaluation of CAM5 simulated black carbon (BC) concentration for the  
1067 period of 2003-2011 (in  $\text{ng g}^{-1}$ ) in the top snow layer against observations in the  
1068 Arctic [Doherty *et al.*, 2010] and Northern China [Wang *et al.*, 2013b]. The top snow  
1069 layer ranges in thickness from 1 to 3 cm. Configuration of the two CAM5 simulations  
1070 (FIRE and NOFIRE) is summarized in Table 1. Panel (a) shows the comparisons at  
1071 different latitudes. The box and whisker plot in panel (b) shows the minimum and  
1072 maximum value with the bar, the 25th and 75th percentiles with the box, the 50th  
1073 percentile (i.e., median) by the bar within the box, and the mean value with the dot.

1074

1075 Figure 10. (a) Annual mean radiative effect due to surface albedo changes ( $\text{RE}_{\text{surf}}$ ,  $\text{W}$   
1076  $\text{m}^{-2}$ ) averaged over the period of 2003-2011 of all fire aerosols over land regions, and  
1077 annual mean surface effect of fire BC-in-snow calculated from SNICAR averaged (b)  
1078 over all times and (c) only when snow is present. The plus signs in (a) denote the  
1079 regions where the radiative effect is statistically significant at the 0.1 level.

1080

1081 Figure 11. Annual mean net shortwave flux changes ( $\text{W m}^{-2}$ ) over the period of  
1082 2003-2011 (a) at top of the atmosphere, (b) in the atmosphere, (c) at surface, and  
1083 changes of (d) surface air temperature (TS, K), (e) convective precipitation ( $\text{mm d}^{-1}$ ),  
1084 and (f) large-scale precipitation ( $\text{mm d}^{-1}$ ) due to all fire aerosols. The plus signs  
1085 denote the regions where the change is statistically significant at the 0.1 level.

1086

1087 Figure 12. Changes in (a) surface air temperature (K), (b) total precipitation ( $\text{mm d}^{-1}$ ),  
1088 (c) cloud liquid water path ( $\text{g m}^{-2}$ ), and (d) low-level cloud cover (%) due to all fire  
1089 aerosols in the boreal summer (JJA) averaged for the period of 2003-2011. The plus  
1090 signs denote the regions where the change is statistically significant at the 0.1 level.

1091

1092



Table 1. Numerical experiments and associated fire aerosol emissions in each experiment.

| Experiment  | Ensembles | Fire BC | Fire POM | Fire SO <sub>2</sub> |
|-------------|-----------|---------|----------|----------------------|
| FIRE        | 10        | On      | On       | On                   |
| NOFIRE      | 10        | Off     | Off      | Off                  |
| NOFIREBC    | 10        | Off     | On       | On                   |
| NOFIREPOM   | 10        | On      | Off      | On                   |
| FIRE_BBFFBF | 1         | On      | On       | On                   |

Table 2. Global, tropics (25°S to 25°N) and Arctic (60°N to 90°N) annual mean fire aerosol (POM and BC) burdens, fire aerosol AOD, total fire aerosol radiative effect (RE) at TOA, radiative effects due to aerosol-radiation interactions (REari), due to aerosol-cloud interactions (REaci), and due to surface albedo changes (REsac), and changes in cloud liquid water path (LWP), low-level cloud cover, net solar fluxes at surface, shortwave atmospheric absorption, surface air temperature, and precipitation (total, convective, and large-scale) due to all fire aerosols. Standard deviations about the 10-ensemble means are included. The change shown in bold character is statistically significant at the 0.05 level.

|  | Global                | Tropics<br>(25°S to 25°N) | Arctic<br>(60°N to 90°N) |
|--|-----------------------|---------------------------|--------------------------|
| Fire POM burden (mg m <sup>-2</sup> )  | <b>1.25 ± 0.01</b>    | <b>1.87 ± 0.01</b>        | <b>1.70 ± 0.08</b>       |
| Fire BC burden (mg m <sup>-2</sup> )   | <b>0.106 ± 0.001</b>  | <b>0.17 ± 0.001</b>       | <b>0.09 ± 0.004</b>      |
| Fire aerosol optical depth   | <b>0.008 ± 0.001</b>  | <b>0.012 ± 0.001</b>      | <b>0.007 ± 0.0004</b>    |
| Total radiative effect (W m <sup>-2</sup> )                                    | <b>-0.55 ± 0.07</b>   | <b>-0.66 ± 0.09</b>       | <b>-1.35 ± 1.03</b>      |
| Radiative effect due to ARI (W m <sup>-2</sup> )                               | <b>0.16 ± 0.01</b>    | <b>0.17 ± 0.017</b>       | <b>0.43 ± 0.028</b>      |
| Radiative effect due to ACI (W m <sup>-2</sup> )                               | <b>-0.70 ± 0.05</b>   | <b>-0.82 ± 0.09</b>       | <b>-1.38 ± 0.23</b>      |
| Radiative effect due to surface albedo changes (over land, W m <sup>-2</sup> ) | 0.03 ± 0.10           | -0.04 ± 0.06              | 0.09 ± 0.80              |
| Cloud liquid water path (g m <sup>-2</sup> )                                   | <b>1.62 ± 0.01</b>    | <b>1.95 ± 0.13</b>        | <b>2.59 ± 0.25</b>       |
| Low-level cloud cover (%)  | 0.012 ± 0.06          | <b>-0.055 ± 0.05</b>      | <b>0.46 ± 0.45</b>       |
| Net solar flux at surface (W m <sup>-2</sup> )                                 | <b>-1.38 ± 0.05</b>   | <b>-1.91 ± 0.12</b>       | <b>-2.27 ± 1.04</b>      |
| Shortwave atmospheric absorption (W m <sup>-2</sup> )                          | <b>0.83 ± 0.03</b>    | <b>1.25 ± 0.04</b>        | <b>0.92 ± 0.05</b>       |
| Surface air temperature (K)  | <b>-0.03 ± 0.03</b>   | <b>-0.024 ± 0.011</b>     | -0.15 ± 0.20             |
| Total precipitation rate (mm day <sup>-1</sup> )                               | <b>-0.010 ± 0.002</b> | <b>-0.016 ± 0.01</b>      | -0.001 ± 0.02            |
| Convective precipitation rate (mm day <sup>-1</sup> )                          | <b>-0.003 ± 0.002</b> | -0.001 ± 0.009            | <b>-0.005 ± 0.003</b>    |
| Large-scale precipitation rate (mm day <sup>-1</sup> )                         | <b>-0.007 ± 0.002</b> | <b>-0.015 ± 0.003</b>     | 0.004 ± 0.019            |

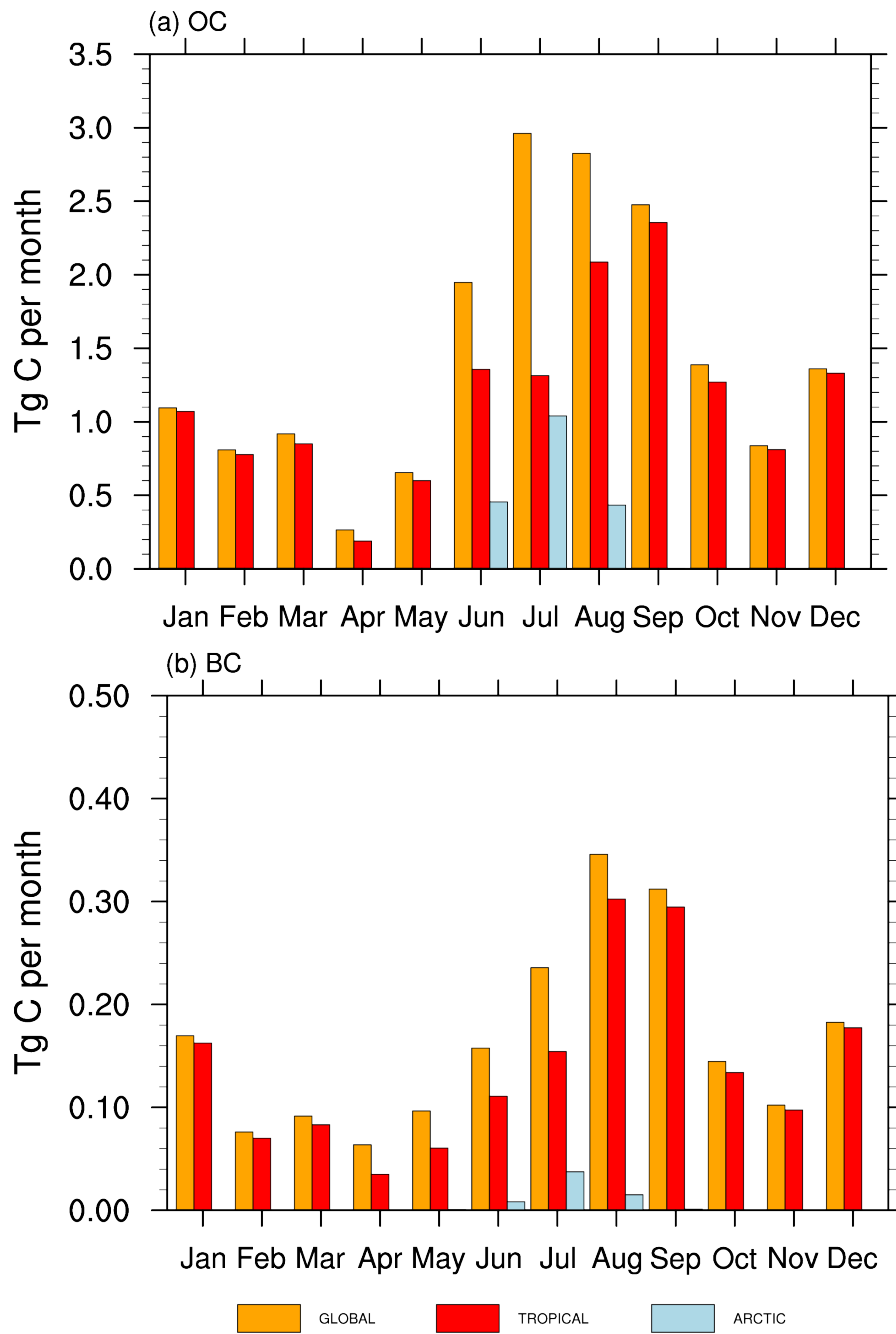


Figure 1. Seasonal variation of GFED monthly fire (a) organic carbon (OC) and (b) black carbon (BC) emissions ( $\text{Tg C month}^{-1}$ ) averaged for the period of year 2003 to 2011 in the global, tropical ( $25^{\circ}\text{S}$  to  $25^{\circ}\text{N}$ ) and Arctic ( $60^{\circ}\text{N}$  to  $90^{\circ}\text{N}$ ) regions.

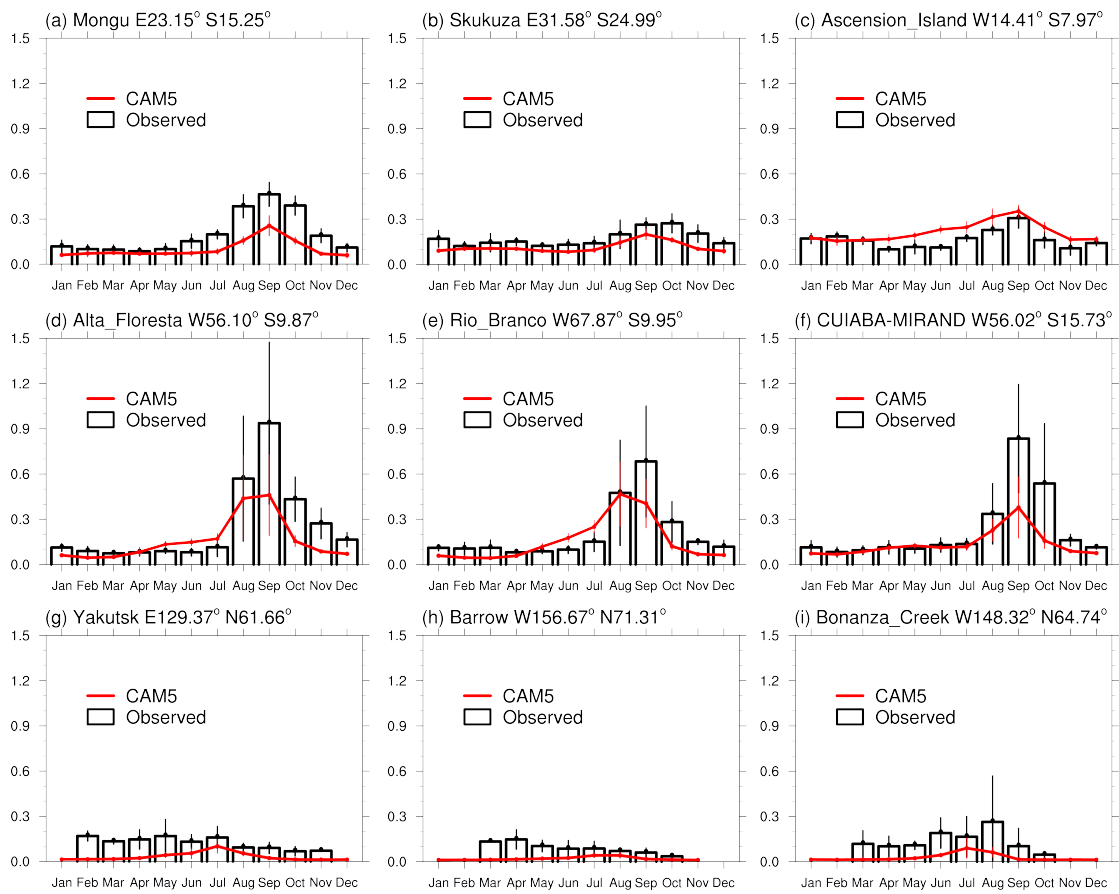


Figure 2. Comparison of modeled seasonal variations of aerosol optical depth (AOD) for the period of 2003-2011 with observations for the same period from the AERONET sites. The upper, middle, and bottom panels represent the sites in southern Africa, South America, and the Arctic, respectively.

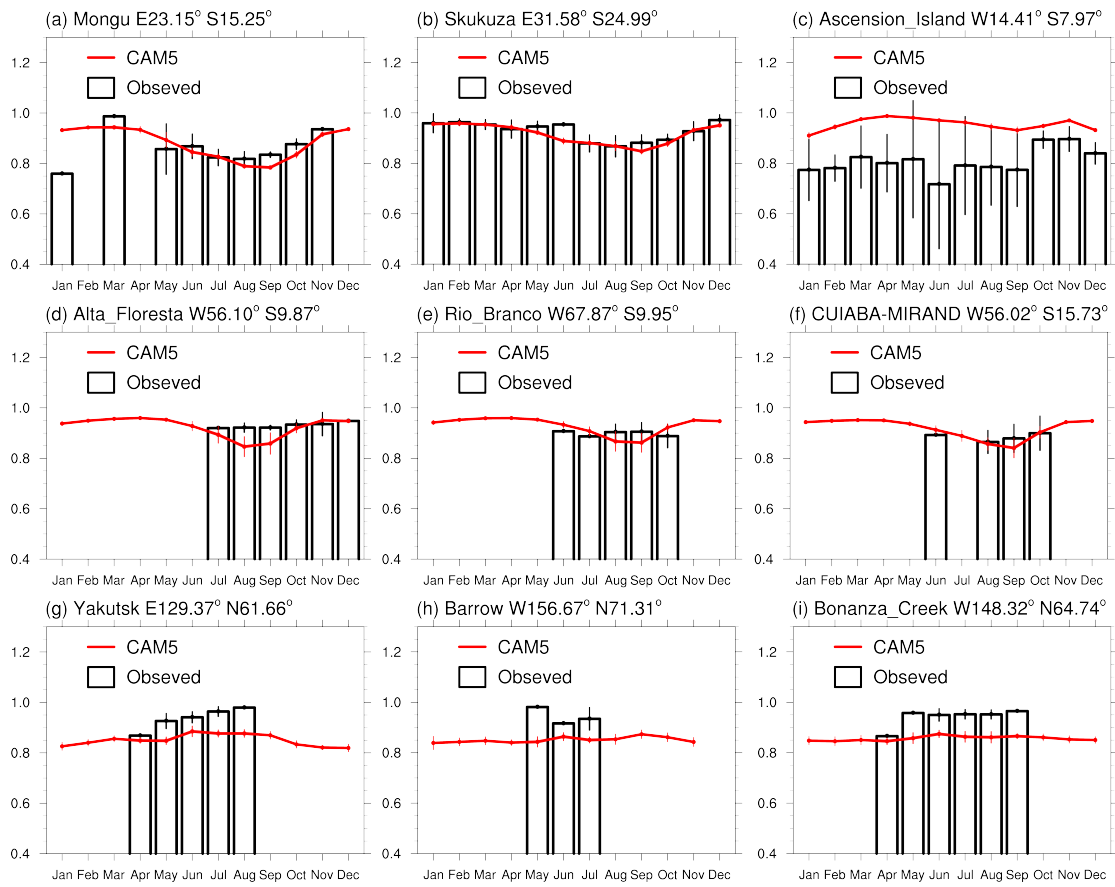


Figure 3. Same as Figure 2, but for the comparison of single scattering albedo (SSA) at 550 nm.

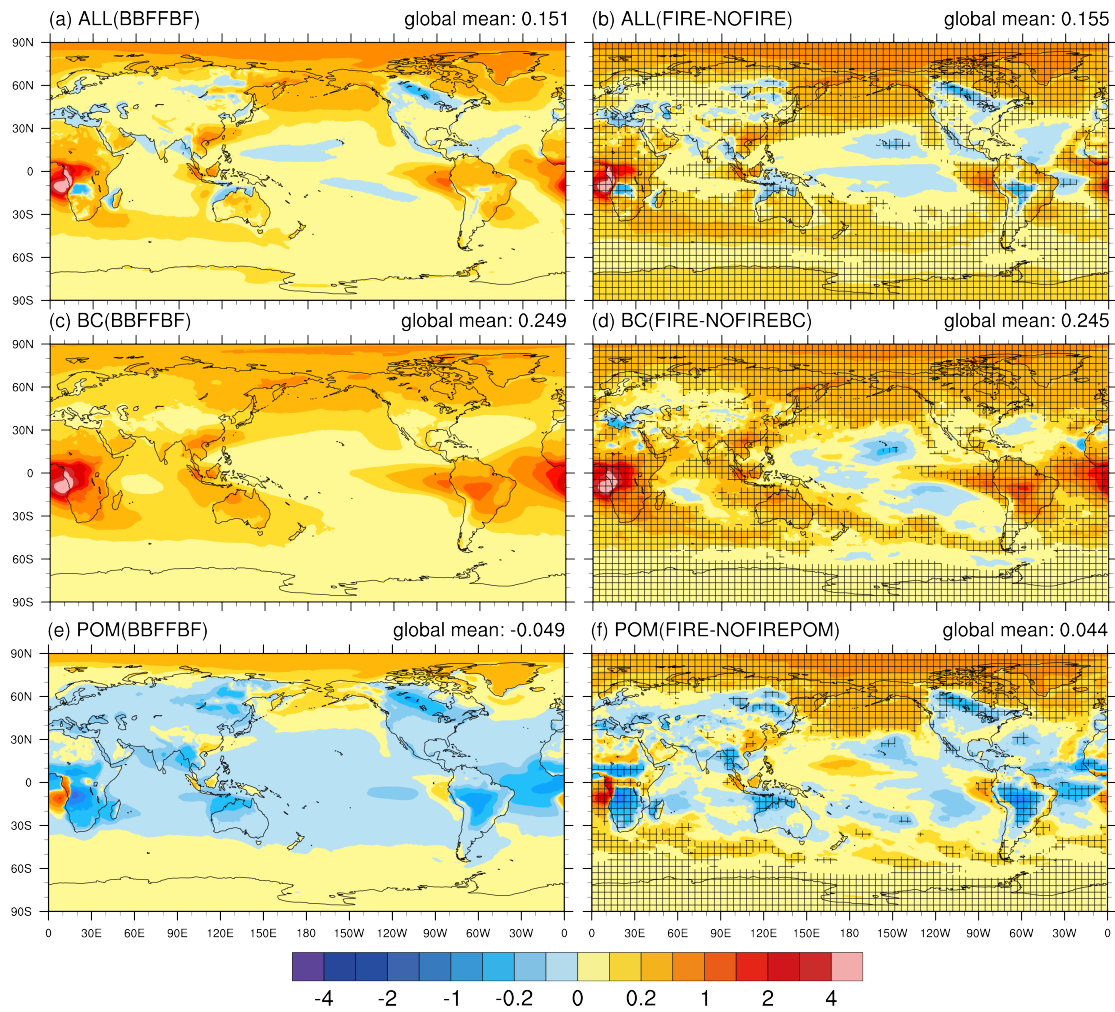


Figure 4. Annual mean radiative effect due to aerosol-radiation interactions ( $\text{RE}_{\text{ari}}$ ) ( $\text{W m}^{-2}$ ) averaged over the period of 2003-2011 due to (a) all fire aerosols, (c) fire BC, and (e) fire POM estimated with the method of BBFFBF (left panels), and with the method of Ghan (2013) ((b), (d), and (f) in the right panels). The plus signs in Figure 4(b), (d) and (f) denote the regions where the radiative effect estimated with Ghan [2013] is statistically significant at the 0.05 level.

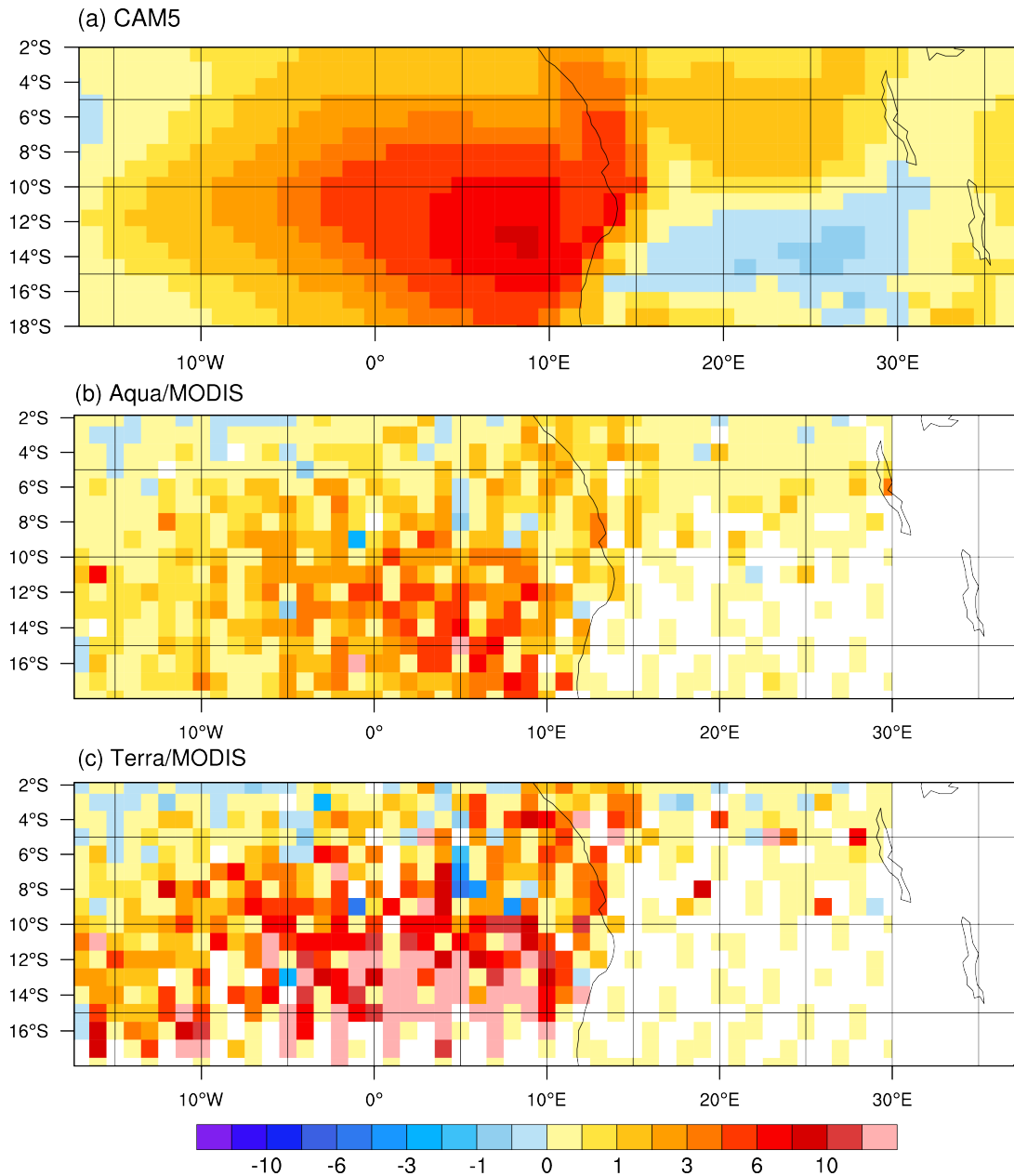


Figure 5. (a) September-October-November (SON) mean fire aerosol radiative effect due to aerosol-radiation interactions (REari) ( $\text{W m}^{-2}$ ) for the period of 2003-2011 over the Southeast Atlantic Ocean due to all fire aerosols. (b) and (c) are the same as (a), but for the above-cloud aerosol REari for the period of 2007-2011 estimated using Aqua/MODIS and Terra/MODIS products [Zhang *et al.*, 2014], respectively.

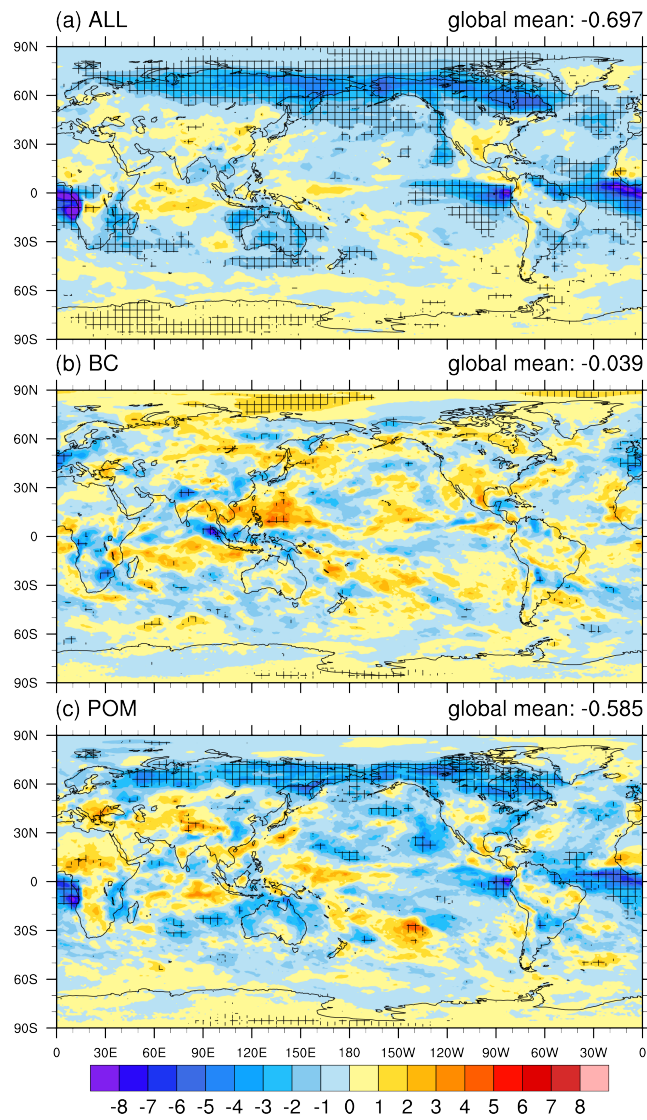


Figure 6. Annual mean radiative effect due to aerosol-cloud interactions (REaci) ( $\text{W m}^{-2}$ ) averaged over the period of 2003-2011 due to (a) all fire aerosols, (b) fire BC, and (c) fire POM. The plus signs denote the regions where the radiative effect is statistically significant at the 0.1 level.



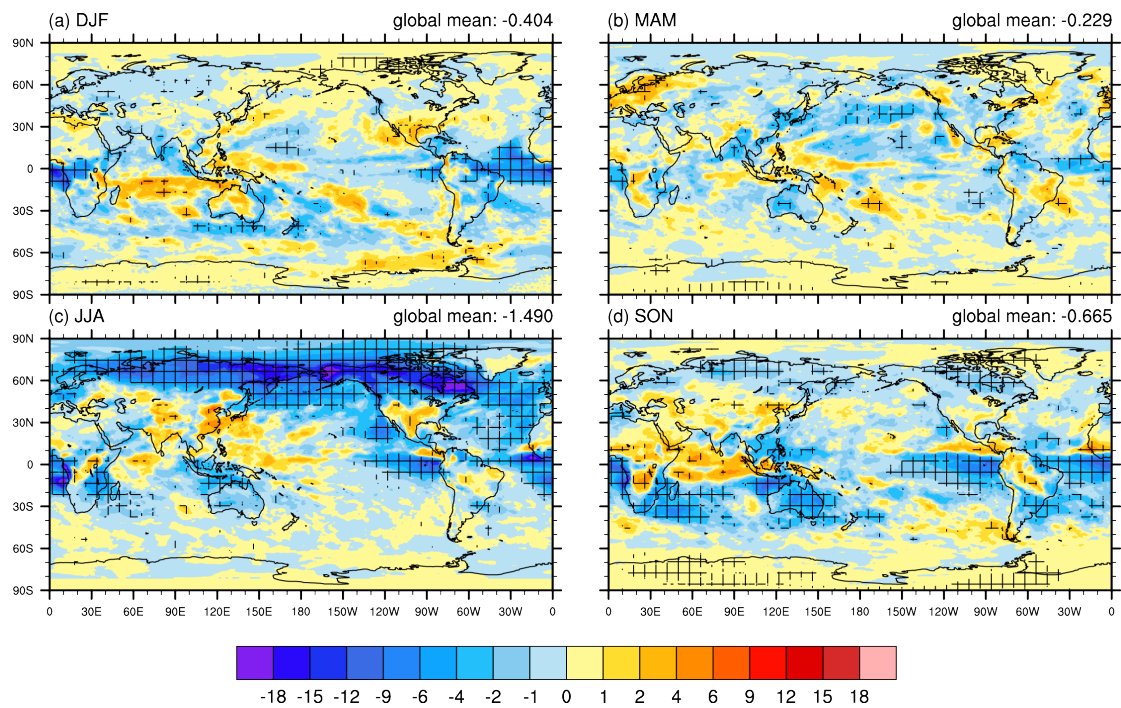


Figure 7. Seasonal variation of radiative effect of all fire aerosols due to aerosol-cloud interactions (REaci) ( $W m^{-2}$ ) for the period of 2003-2011 for (a) December-January-February (DJF), (b) March-April-May (MAM), (c) June-July-August (JJA), and (d) September-October-November (SON). The plus signs denote the regions where the radiative effect is statistically significant at the 0.05 level.

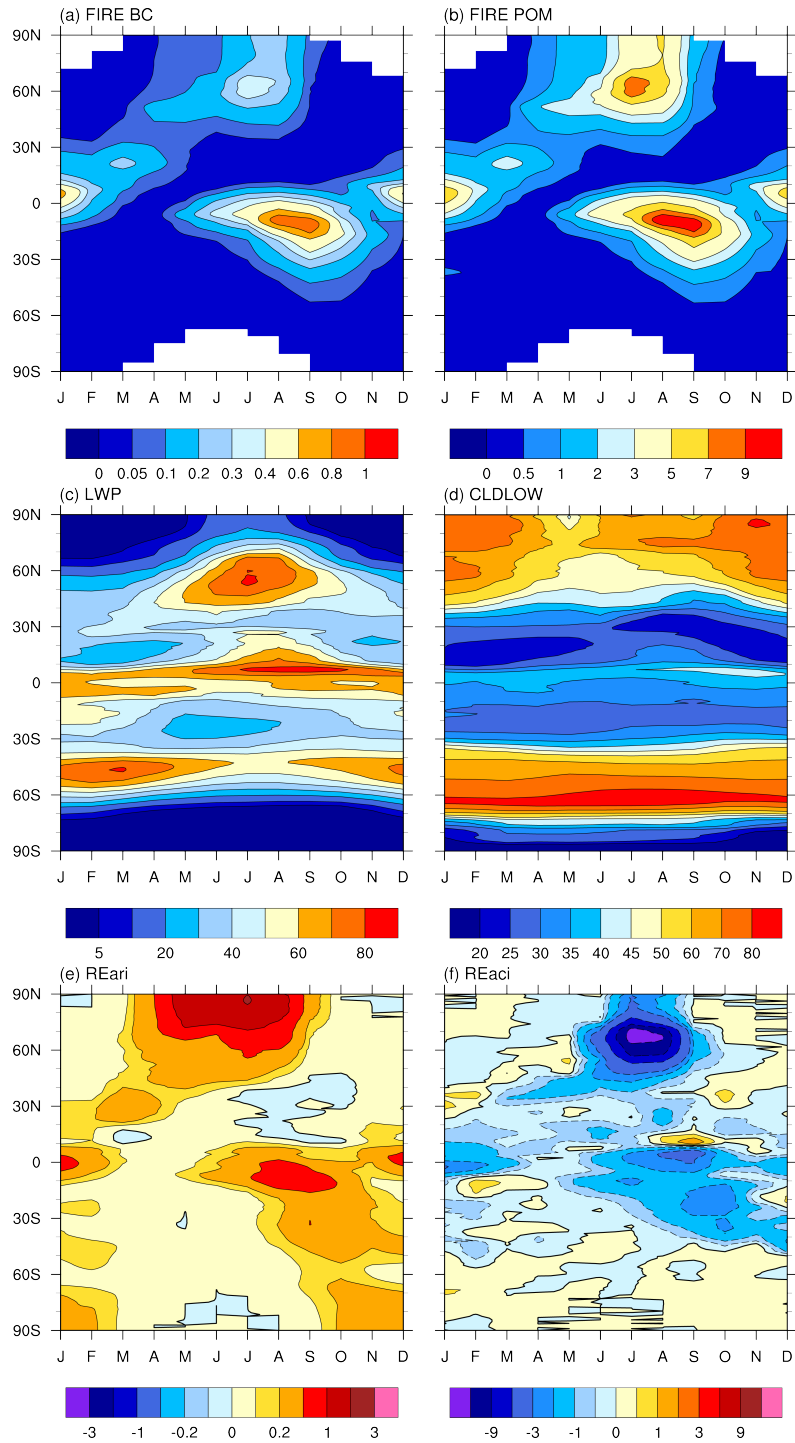


Figure 8. Month-latitude cross sections of zonal mean and monthly (a) vertically-integrated concentrations ( $\text{mg m}^{-2}$ ) of fire BC and (b) fire POM, (c) cloud liquid water path (LWP, in  $\text{g m}^{-2}$ ), (d) low-level cloud cover (CLDLLOW, in %), (e) radiative effect due to aerosol-radiation interactions (REari, in  $\text{W m}^{-2}$ ), and (f) radiative effect due to aerosol-cloud interactions (REaci, in  $\text{W m}^{-2}$ ) of all fire aerosols.

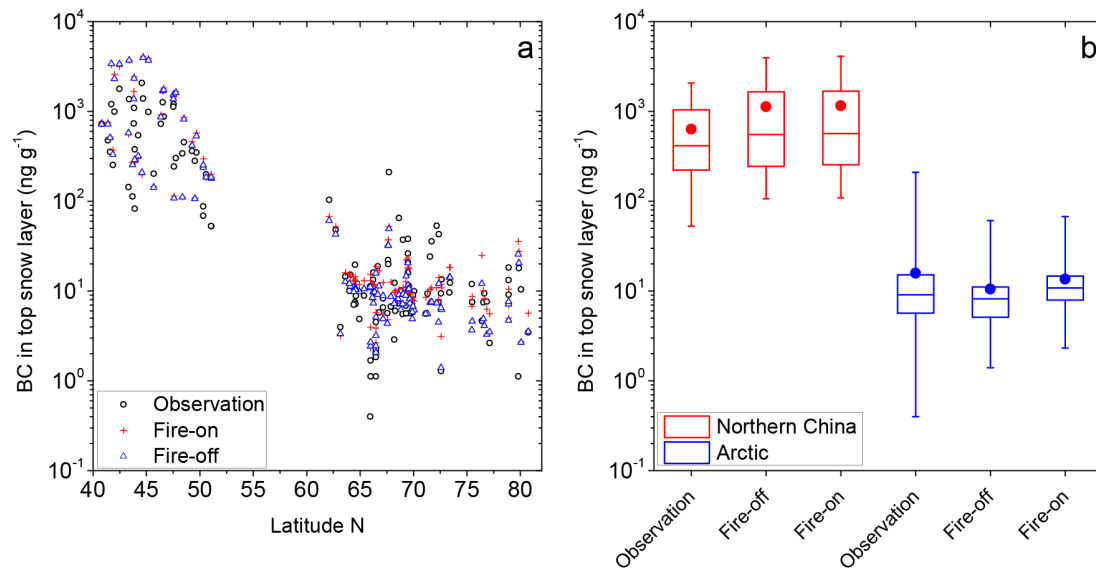


Figure 9. Evaluation of CAM5 simulated black carbon (BC) concentration for the period of 2003-2011 (in  $\text{ng g}^{-1}$ ) in the top snow layer against observations in the Arctic [Doherty *et al.*, 2010] and Northern China [Wang *et al.*, 2013b]. The top snow layer ranges in thickness from 1 to 3 cm. Configuration of the two CAM5 simulations (FIRE and NOFIRE) is summarized in Table 1. Panel (a) shows the comparisons at different latitudes. The box and whisker plot in panel (b) shows the minimum and maximum value with the bar, the 25th and 75th percentiles with the box, the 50th percentile (i.e., median) by the bar within the box, and the mean value with the dot.

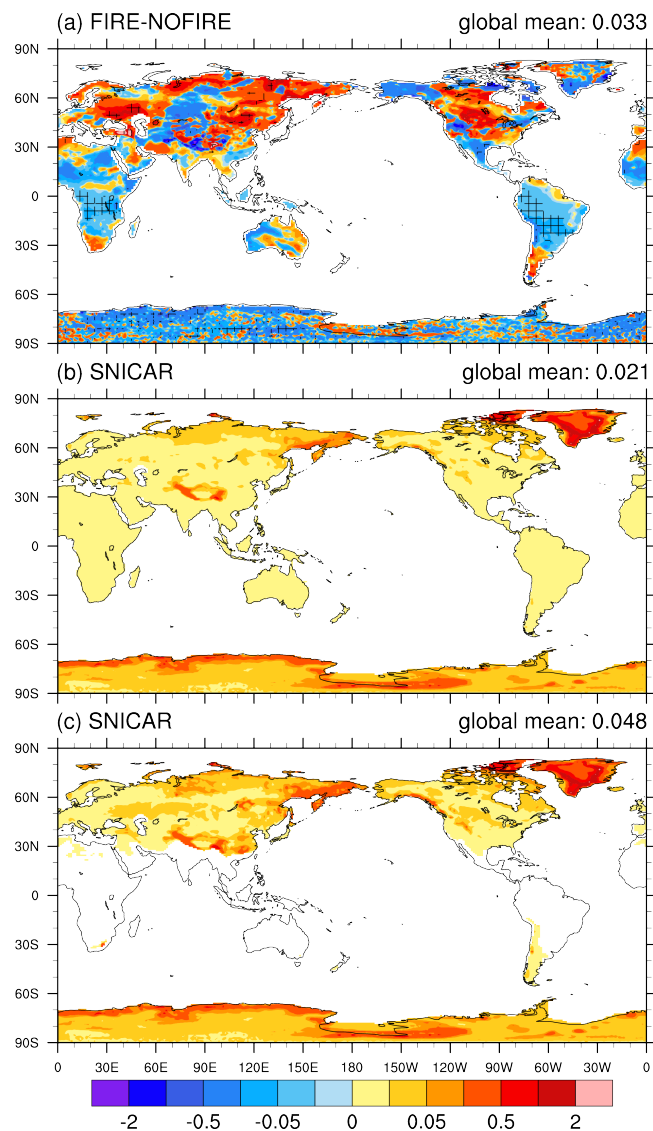


Figure 10. (a) Annual mean radiative effect due to surface albedo changes ( $RE_{sac}$ ,  $W m^{-2}$ ) averaged over the period of 2003-2011 of all fire aerosols over land regions, and annual mean surface effect of fire BC-in-snow calculated from SNICAR averaged (b) over all times and (c) only when snow is present. The plus signs in (a) denote the regions where the radiative effect is statistically significant at the 0.1 level.

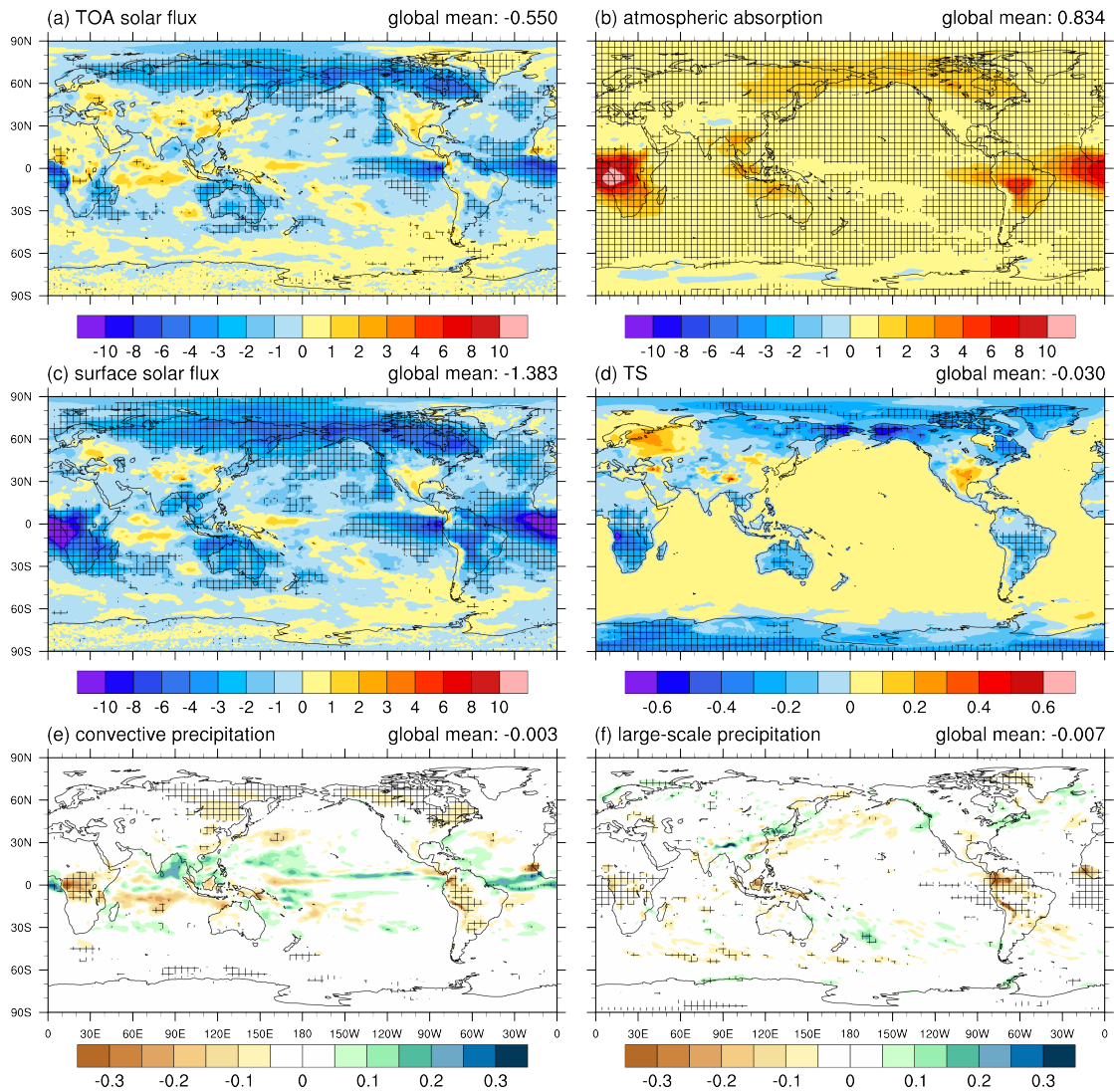


Figure 11. Annual mean net shortwave flux changes ( $\text{W m}^{-2}$ ) over the period of 2003-2011 (a) at top of the atmosphere, (b) in the atmosphere, (c) at surface, and changes of (d) surface air temperature (TS, in K), (e) convective precipitation ( $\text{mm d}^{-1}$ ), and (f) large-scale precipitation ( $\text{mm d}^{-1}$ ) due to all fire aerosols. The plus signs denote the regions where the change is statistically significant at the 0.1 level.

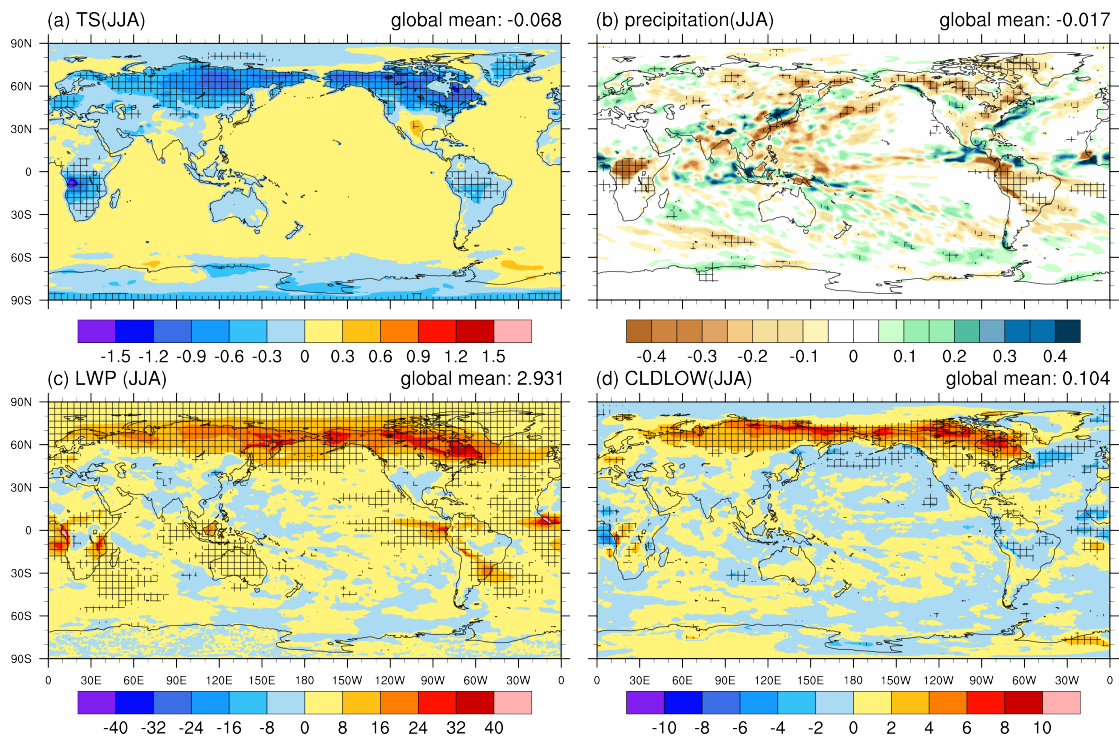


Figure 12. Changes in (a) surface air temperature (TS, in K), (b) total precipitation ( $\text{mm d}^{-1}$ ), (c) cloud liquid water path (LWP, in  $\text{g m}^{-2}$ ), and (d) low-level cloud cover (CLDLow, in %) due to all fire aerosols in the boreal summer (JJA) averaged for the period of 2003-2011. The plus signs denote the regions where the change is statistically significant at the 0.1 level.